Wiley
Structural Control and Health Monitoring
Volume 2026, Article ID 3858095, 22 pages
https://doi.org/10.1155/stc/3858095

WILEY

Research Article

Monitoring Bridge Vibrations via Spaceborne SAR Micro-Doppler

Alessandro Lotti,[1] **Aleksanteri B. Vattulainen**,[2] **Sebastian Diaz Riofrio**,[2] **Chiara Suppi**,[1] **Enrico Tubaldi**,[3] **Daniele Zonta**,[1] **Pietro Milillo**,[4,5] **and Carmine Clemente**[2]

[1]*Department of Civil, Environmental and Mechanical Engineering, University of Trento, Trento, Italy*
[2]*Department of Electronic and Electrical Engineering, University of Strathclyde, Glasgow, UK*
[3]*Department of Civil and Environmental Engineering, University of Strathclyde, Glasgow, UK*
[4]*Department of Civil and Environmental Engineering, University of Houston, Houston, Texas, USA*
[5]*Microwaves and Radar Institute, German Aerospace Center (DLR), Weßling, Germany*

Correspondence should be addressed to Alessandro Lotti; alessandro.lotti@unitn.it

Received 9 September 2025; Revised 24 November 2025; Accepted 4 December 2025

Academic Editor: Lukasz Jankowski

The advent of Synthetic Aperture Radar (SAR) imaging has presented the possibility of remote monitoring of civil infrastructure on a large scale. Although well established for observing slow and long-term phenomena, its application to vibration-based structural health monitoring (SHM) remains relatively unexplored in the current literature. This study demonstrates the use of micro-Doppler SAR (MDSAR) using data from spaceborne platforms for measuring structural vibrations of a real bridge, specifically the line of sight velocity time histories of the deck. These measurements are compared to synchronous ground truth data to validate the method and assess its accuracy. Experimental results show that MDSAR measures vibration with an error in velocity on the order of 1 mm/s and successfully identifies the bridge's dominant frequencies from two separate SAR acquisitions at different times. Spectral correlation with ground truth data reaches values up to 0.88. Frequency estimation errors are essentially controlled by the resolution of the spectrum, which in turn is limited by the acquisition time. In this work, a frequency resolution of 0.06 Hz is achieved for an acquisition duration of 16 s. Given these results, it is expected that MDSAR could be suitable for monitoring natural frequencies and performing modal recognition for bridges. Further improvements in the technology and in the analysis algorithm could potentially enable the accurate measurement of mode shape components.

Keywords: micro-Doppler; micromotion; modal extraction; SAR; structural health monitoring

1. Introduction

Vibration-based structural health monitoring (VBSHM) methods, which typically rely on conventional contact sensors such as accelerometers, are widely used for assessing the structural state of civil infrastructure [1]. VBSHM has long been the subject of research, with numerous studies aimed at identifying damage from vibrational features. The literature includes several comprehensive reviews that collect a variety of traditional methods used for diagnostics and damage detection [2–6]. Although contact measurement approaches have been proven to be effective, they also face significant limitations, which have led to the exploration of remote sensing alternatives.

Firstly, the installation of sensors directly on a structure, such as a bridge, poses logistical challenges [7]. Deploying accelerometers or similar devices often requires safety precautions, traffic disruptions, and specialized workers, which collectively inflate costs and delay the operational readiness of the monitoring system. Moreover, maintaining and calibrating sensor networks introduce further complexity and long-term expenses [8]. This becomes problematic when dealing with large-scale infrastructure, where a large number of sensors are needed to achieve sufficient spatial coverage [9]. For example, the Mezcala cable-stayed bridge was instrumented with a total of 124 sensors (including accelerometers and other sensor types) at an

estimated cost of USD 1.8 million, covering both installation and maintenance over an operating period of 30 years [10]. Secondly, in regions with a high concentration of aging infrastructure—where safety concerns are important and widespread monitoring is promptly needed—conventional VBSHM becomes impractical [11], especially when resources are limited. To overcome these challenges, the focus of research has increasingly shifted toward remote sensing for SHM [12], as these technologies do not require the physical installation of the sensor on the structure. Several solutions, each based on different physical principles, exist and have been studied, including the use of uncrewed aerial vehicles (UAVs) [13–15], laser vibrometers [16], light detection and ranging (LiDAR) [17, 18], and ground-based Doppler radars [19–21]. As an alternative to these approaches, SAR satellite remote sensing is of particular interest due to its unique capabilities. SAR is a radar imaging technique capable of producing high-resolution images of the Earth's surface. Unlike optical sensors, which passively capture reflected sunlight, SAR systems (as well as other active sensors like ground-based radar and LiDAR) actively illuminate the scene and measure the backscattered electromagnetic signal, which is parameterized in terms of its reflectivity (magnitude) and phase. The signal carries information about the surface geometry, the electromagnetic properties, the distance between the radar and the surface targets, and the relative motion between the sensor and the target—the latter two being part of the measured phase, which is a property fundamental for generating the SAR image and particularly relevant for this work. A major advantage of SAR lies in its ability to capture large areas (typically many square kilometers) while maintaining high quality imaging capability. Moreover, the cost of SAR imagery is rapidly decreasing thanks to the advent of commercial providers on the scene. Generally, prices range from a few hundred up to a few thousand USD (e.g., up to 3000–5000 USD [22]), depending on spatial resolution and revisit time (i.e., the time interval between successive acquisitions). In some cases, SAR data are freely available, such as from the Sentinel-1 mission [23].

In the context of SHM, one technique making use of the benefits of SAR is interferometric SAR (InSAR). InSAR is a method that compares the phase information of successive SAR acquisitions to detect and quantify surface displacements in the image over time [24, 25]. In previous years, advanced multitemporal InSAR techniques, such as persistent scatterer interferometry (PSI) and small baseline subset (SBAS), have been developed to monitor surface deformation [26] with millimeter-level accuracy [27]. As a result, InSAR has been increasingly applied and validated in civil engineering applications for SHM. The literature case studies include long-term monitoring of dam foundations [28], bridge deflections [27], and even detection of scour-related features [29]. Another benefit of SAR technology is its archive of historical data, enabling retroactive analyses of collapsed infrastructure [30] and supporting the development of early warning systems for risk assessment [31]. Despite these advantages, InSAR has limitations that restrict its use for certain SHM tasks:

- It is effective for measuring slow, long-term deformations, but it is not suited for rapid and bulk movements [32];
- InSAR requires a large number of acquisitions for reliable results [33] and cannot measure displacements from a single SAR image;
- The temporal resolution of InSAR depends on the revisit time of the satellite, which is typically on the order of days.

Due to these limitations, InSAR cannot be used to assess the vibrational behavior of structures; however, a different class of techniques exists that works on single-pass (i.e., individual) SAR acquisitions and is capable of detecting vibrational information. These approaches exploit micro-Doppler (m-D) effects induced by target motion and are the focus of this study.

When a moving target is illuminated by a radar signal, the backscattered signal is subjected to a phase shift due to the Doppler effect [34], a well-known phenomenon caused by the relative motion between the sensor and the target. Standard SAR processing assumes the scene to be static, producing accurate images of stationary ground targets. When targets move during an acquisition (or vibrate, as for civil infrastructure components), uncompensated phase shifts are introduced into the receiving signal, generating artifacts in the final SAR image. These artifacts can be grouped into two types, depending on the nature of the motion: Doppler, caused by translational movement, and m-D, caused by periodic or oscillatory micromotions (m-m) of the target [34]. Consequently, the m-D effect in SAR imagery carries kinematic information of targets such as vibrations [35], presenting the opportunity to reconstruct structural dynamics from single-pass SAR acquisitions. Several MDSAR techniques have been developed to measure m-D information from SAR imagery, where some of these have been applied to the field of civil engineering SHM. For a comprehensive review of MDSAR methods and their working principles, the reader is referred to the recent literature review by Rollo et al. [36]. In the following, selected publications on measuring vibrational features from m-D signatures in SAR data are reported. Initial works focused mainly on demonstrating the potential of the m-D extraction techniques under controlled environments, using isolated vibrating corner reflectors (CRs) mounted on shaker devices to replicate vibration without interference from the surroundings. For example, Chen et al. [37] measured a vibration frequency of 2.3 Hz from a CR on a shaker, with an error of 0.3 Hz with respect to ground truth, although amplitude estimates were not reported. Ruegg et al. [35] studied the effects of both vibrating and rotating targets and successfully extracted a 1-Hz frequency from a rotating CR. Recently, Clemente et al. [38] and Rollo et al. [39] applied tracking and backprojection techniques to reconstruct vibrations with a frequency of 2 Hz and a vertical amplitude of 15 mm, validated against synchronous ground measurements. Finally, Lotti et al. [40] conducted experiments across a wide range of frequencies and amplitudes, extending

measurements beyond simple case studies. This work included an experimental validation based on synchronous ground truth measurements and demonstrated that vibrations comparable to those found in civil infrastructure could be captured with SAR.

While m-D approaches are less mature than InSAR in the context of civil SHM, they have also been applied to real-world case studies employing methods such as the subpixel offset tracking (SPOT). Biondi et al. [41] used SPOT to identify cracks in the Mosul Dam, based on vibrational anomalies reconstructed from SAR imagery, and validated these crack locations with those obtained from the PSI InSAR technique. In a later work, Biondi et al. [42] examined several bridge case studies, detecting anomalies in the vibrational behavior of the structures as determined by SAR m-m measurements. This investigation successfully identified locations of cracks and expansion joints in the deck, which were validated with photographic documentation. Focsa et al. [43] retrieved the natural frequencies of a bridge using an MDSAR method, reporting errors ranging from 0.03 to 0.5 Hz; however, the actual accuracy remains uncertain as the comparison relied on asynchronous ground-based radar measurements, and multiple spectral peaks were identified nearby the true frequencies. Recently, Vattulainen et al. [44] employed a modified backprojection algorithm (BPA)—an MDSAR technique distinct from SPOT—to estimate the dominant frequency on a bridge, reporting an error of 0.04 Hz validated against synchronous measurements. However, their work only focused on a frequency-domain comparison and did not cover a time history reconstruction of the vibrations.

In summary, m-D SAR techniques offer a promising alternative to traditional VBSHM methods, enabling vibrational information to be measured both remotely and over large areas from single-pass SAR images. Prior studies have largely focused on controlled experiments, and real-world validation remains limited. Notably, no previous study has applied MDSAR to a full-scale civil structure while directly validating measured vibrations against synchronous ground truth data in the time domain. A comprehensive metrological evaluation of any MDSAR technique, including SPOT, is still missing. Furthermore, the possibility of using SAR data for modal extraction, specifically for identifying natural frequencies and mode shapes, remains largely unexplored.

The objective of this study is to address the following research questions:

i. Can MDSAR be used to measure the vibration time series of a real-world structure?
ii. In the context of a real-world structure, how accurate are these measurements, and what are the limitations of the technique?
iii. What are the future possibilities for extracting modal parameters from spaceborne SAR data?

To explore these questions, the case study of the South Portland St. Suspension Bridge in Glasgow, UK, is considered. While this paper focuses on the measurement of vibrations and qualitatively discusses the extraction of individual modal parameters (i.e., natural frequencies and mode shapes) from SAR data, a detailed approach to a proper modal extraction will be presented in a future publication. This work constitutes a significant advancement in the use of SAR for VBSHM. It presents the first metrological assessment of a SAR-based micro-Doppler method for measuring the vibrations of a real, instrumented bridge under operational conditions. By comparing the SAR-derived velocities against synchronous ground truth measurements, this study confirms the potential of this technique and identifies its current limitations.

The remainder of this paper is structured as follows. Section 2 provides the necessary background for SAR-based vibration monitoring, including an overview of SAR principles and the effects of moving objects in SAR images. It then introduces the SPOT algorithm, covering azimuth subaperture segmentation, subpixel tracking, and velocity time history reconstruction. The section continues with a description of the South Portland St. Suspension Bridge case study, followed by the layout of the contact-based accelerometer system used for validation and the methodology used to compare SAR-derived results with ground-truth data. Section 3 presents and discusses the experimental results. It begins by evaluating the SAR-measured vibrations against the ground-truth data using various metrics. It then addresses the three key research questions of the study and discusses current limitations and potential improvements for modal extraction using SAR. Finally, Section 4 summarizes the main findings and outlines current challenges while proposing directions for future developments.

2. Materials and Methods

2.1. Principles of SAR Technology. A SAR operates by transmitting and receiving radar pulses while traveling at a velocity v_p on a moving platform, which in this case is a satellite. SAR signals are EM waves with much longer wavelengths (see Table 1) than those used by optical sensors, and since they are active sensors, SAR systems are not dependent on sunlight or weather conditions.

Typically, a SAR acquisition spans several seconds for a duration t_a and involves the sensor collecting backscattered radar pulses while illuminating the same ground target from multiple positions along the flight path. The processing of the data—to account for the different phase changes for each pulse due to the moving platform—*synthesizes* the antenna (or aperture), hence the term *synthetic aperture* in SAR. The SAR sensor is tilted with an incidence angle, θ, with respect to the vertical direction of the surface, and the radial distance from the ground target (e.g., the bridge being monitored) to the sensor is referred to as the slant-range distance, $R(t)$; this direction is often referred to as the line of sight (LOS) of the sensor. Figure 1 shows the orbit geometry for a specific acquisition mode, known as spotlight mode, which is discussed later in this section.

SAR images are complex valued matrices, where each pixel contains both a magnitude and a phase component. The magnitude and phase represents the reflectivity (i.e., intensity) and the delay of the backscattered signal,

Table 1: Radar frequency bands commonly used in SAR systems, with their associated frequency and wavelength values [45].

Band	Central frequency (GHz)	Wavelength (cm)
L	1-2	15–30
S	2–4	7.5–15
C	4–8	3.8–7.5
X	8–12	2.4–3.8

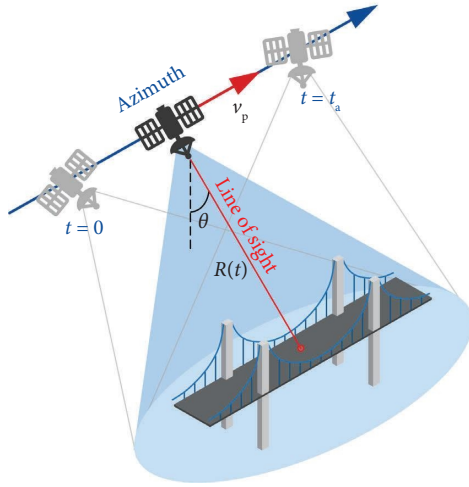

Figure 1: SAR spotlight mode acquisition geometry, showing the start $t = 0$ and end $t = t_a$ times of the acquisition, the platform velocity v_p, the incidence angle θ, and the slant-range distance $R(t)$ between the sensor and the ground target.

respectively. Figure 2 shows an example of a reflectivity map from spotlight acquisition of the Golden Gate Bridge compared to the corresponding optical image. In general, the reflectivity is affected by the type of the material and shapes of targets; metallic objects with sharp geometries are prominently visible in the reflectivity map. The resulting complex-valued matrix is arranged in *range-azimuth* coordinates. The range direction corresponds to the radial direction from the sensor to the ground target (the slant-range), while the azimuth direction aligns with the platform flight path. The resolution of the reflectivity map (i.e., the size of the pixel in azimuth and range) is defined by the azimuth resolution, Δx, and the range resolution, Δy. Both these quantities depend on the wavelength of the transmitted signal, λ, with the azimuth resolution additionally depending on the acquisition time, t_a.

Several types of acquisition mode exist, each with different trade-offs between resolution and spatial coverage [46]. In this paper, spotlight acquisitions are used, with durations ranging between 5 and 30 s. In this mode, the radar beam is continuously steered ("squinted") such that it remains centered on the same area for the entire acquisition duration. Spotlight mode offers improved azimuth resolution thanks to the extended illumination time, but with reduced spatial coverage compared to other acquisition modes. Nonetheless, spotlight scenes can span areas ranging from 5 to 20 km, enabling the monitoring of multiple structures within a single image while providing finer azimuth resolution. As these acquisitions target specific areas, they are usually not available through archive data sources and must be tasked specifically.

The azimuth resolution for a spotlight acquisition is described by the following equation:

$$\Delta x = \frac{\lambda R(t)}{2 v_p t_a}, \tag{1}$$

where the parameters are as previously defined.

2.1.1. Micromotion in SAR Imagery. Standard SAR processing is designed to produce high-resolution images of static scenes. As discussed in Section 1, targets undergoing some micromotion during the acquisition period will cause characteristic artifacts in the SAR image. This phenomenon is known as the m-D effect and arises from small variations in the radial velocities relative to the SAR moving platform. In general, when a target moves at constant speed, the relative motion in the LOS direction causes an azimuth shift of the target from its true position due to the Doppler effect [34]. The azimuth shift, $x(t)$, due to constant radial velocity, v_r, of the ground target along the LOS is approximated by the relationship shown in the following equation [47].

$$x(t) = -\frac{v_r R(t)}{v_p}. \tag{2}$$

In the case of a target vibrating around a static equilibrium position, the azimuth shifts in the resulting image will appear as *ghost targets* (or *paired echoes*) along the azimuth direction, centered on the true position of the target. These artifacts result from target m-m that induces periodic time-varying changes in the radial velocity. The higher the velocity of vibration, the greater the separation between these paired echoes from the true location. Figure 3(a) shows a clear example of this effect for a single scattering point, given by a CR oscillating vertically with a constant frequency of 1 Hz, and an amplitude of 10 mm. The periodic motion generates a symmetric distribution of the echoes, observable in the reflectivity map.

It is important to note that m-m effects are best preserved in single-look data such as Single-Look Complex (SLC) images, which contain both amplitude and phase information from a single, unaveraged observation throughout the entire acquisition time. While Multi-Look Complex (MLC) products are commonly used in downstream applications due to their reduced speckle noise and lower storage requirements, they are generated by averaging independent looks, which both degrades azimuth resolution and corrupts motion information, making MLC unsuitable for micromotion analysis. In general, motion measurements need full-resolution SLC images or even lower-level products such as raw or Complex Phase History Data (CPHD) to preserve the phase modulations of interest. In this study, SLC imagery was selected as it provides the necessary requirements for m-m extraction, while remaining significantly less demanding in terms of memory and processing resources compared to raw or CPHD formats.

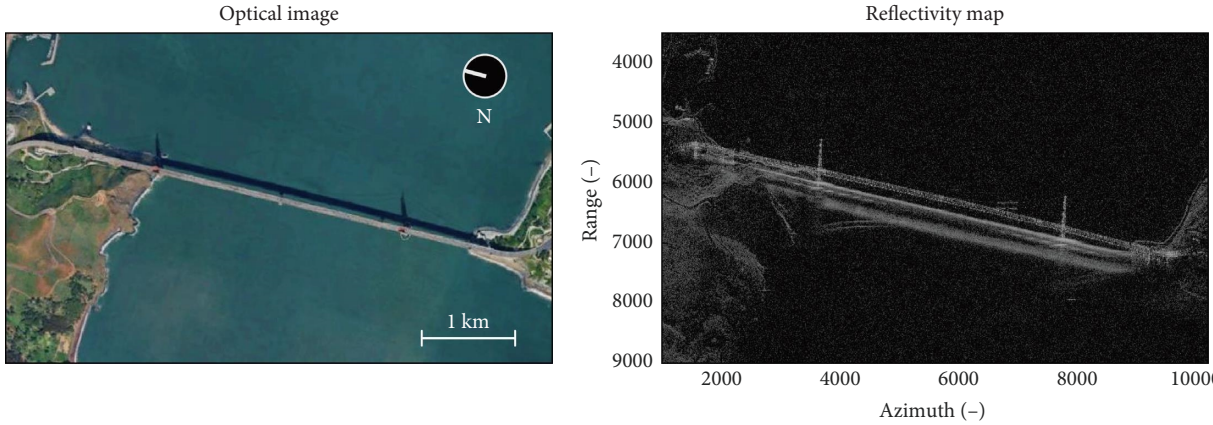

FIGURE 2: A comparison between (a) optical and (b) SAR reflectivity maps of the Golden Gate Bridge from a spotlight acquisition by the Umbra-04 sensor (λ = 31 mm, date: March 25 2023).

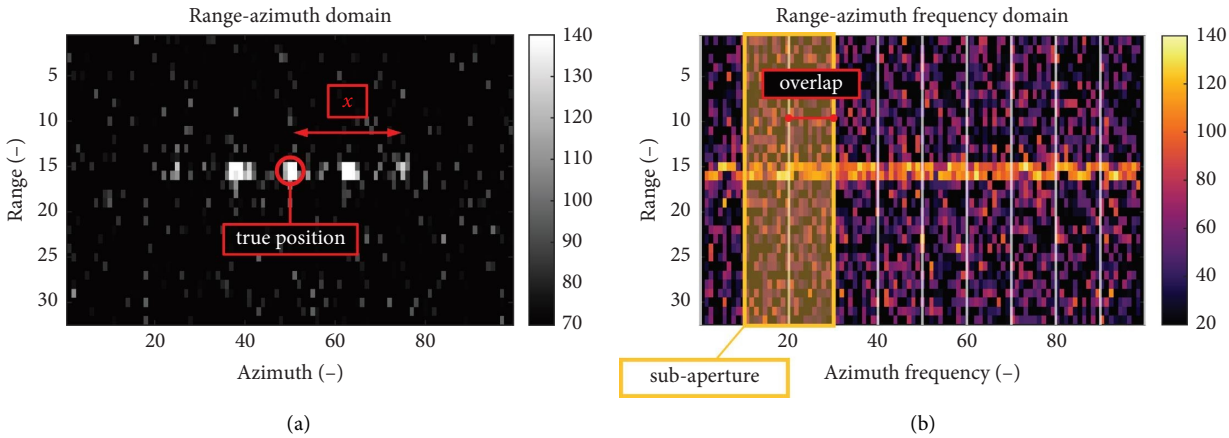

FIGURE 3: Example of micromotion effects in a TerraSAR-X acquisition (Trento, 18 December 2023, 17:09:29 UTC) of a vertically vibrating isolated target (1 Hz, 10 mm). (a) Ghost targets in the *range–azimuth* image; (b) *range-azimuth* frequency representation showing subaperture segmentation (yellow) and overlapping data sections (red).

2.2. SPOT. The technique used in this study is inspired by the work of Biondi et al. [41] and enables the extraction of radial velocity time histories from ground targets from a focused SLC image. The main processing stages are described below.

2.2.1. Range-Azimuth Frequency Transformation. Starting from the SLC matrix in range-azimuth coordinates, a fast Fourier transform (FFT) is applied along the azimuth dimension. This results in a matrix in *range-azimuth frequency* coordinates, as shown in Figure 3(b). The resulting matrix already contains features related to the target vibration.

2.2.2. Subaperture Segmentation. The *range-azimuth frequency* matrix is then split into partially overlapping azimuth subapertures as shown in Figure 3(b). Each subaperture represents a temporal window of the full aperture (t_a), with a relative width controlled by the *aperture fraction*:

$$\alpha = \frac{t_{\text{sap}}}{t_a}, \tag{3}$$

where t_{sap} is the subaperture duration. Adjacent subapertures can be processed to share a portion of the azimuth frequency domain data and therefore be overlapping in time, as described by the *overlap ratio*:

$$\Omega = \frac{t_{\text{ol}}}{t_{\text{sap}}}, \tag{4}$$

where t_{ol} is the overlap duration between adjacent subapertures. Given α and Ω, the total number of subapertures, N, produced is given in the following equation.

$$N = \frac{\alpha^{-1} - \Omega}{1 - \Omega}. \tag{5}$$

2.2.3. Range-Azimuth Transformation. Each *range-azimuth frequency* subaperture is transformed back to the spatial

domain via an inverse FFT (IFFT), resulting in a series of N *range-azimuth* images that are temporally spaced. Specifically, the time vector assigned to the subapertures consists of N linearly spaced values, starting at $t_{\text{sap}}/2$ and ending at $(t_a - t_{\text{sap}})/2$. This ensures that each image corresponds to the center time of its respective subaperture window, resulting in a temporal resolution, Δt, as shown in the following equation.

$$\Delta t = \frac{t_a - t_{\text{sap}}}{N - 1}. \tag{6}$$

It is important to note that by segmenting the full-aperture image into multiple subapertures of duration t_{sap} (shorter than the full acquisition time t_a), the azimuth resolution will degrade due to the reduced observation time. It is possible to preserve the pixel spacing by applying zero padding during the IFFT to upsample each subaperture when moving to the range-azimuth domain. In this way, the granularity of the original image is maintained, although the degradation in image interpretability remains visible. Figure 4 shows examples of reflectivity maps of subapertures from a SAR acquisition over the South Portland St. Suspension Bridge, illustrating the effect of different aperture fractions: $\alpha = 1$ $(t_{\text{sap}} = t_a)$, $\alpha = 0.1$ $(t_{\text{sap}} = 0.1\, t_a)$, and $\alpha = 0.01$ $(t_{\text{sap}} = 0.01\, t_a)$. The figure demonstrates how decreasing the subaperture time progressively degrades the azimuth resolution of the reflectivity map.

2.2.4. Pixel Tracking and Velocity Estimation. A target that is moving with a radial velocity v_r will appear displaced along the azimuth by a distance x determined by equation (2). If the velocity varies over time, the shift x will also change in different subapertures. These displacements are tracked using 2D cross-correlation, applied to patches centered around the target in each subapertures. Cross-correlation is performed relative to a chosen reference subaperture, which in this work is selected as the central subaperture. This results in a time series of azimuth displacements $x(t)$, representing the shift of the target over successive subapertures relative to the reference image.

The corresponding radial velocity time history is then computed by inverting the azimuth shift equation (2):

$$v_r(t) = -\frac{x(t)\, v_p}{R_{\text{ref}}}, \tag{7}$$

assuming the platform velocity and the slant-range distance of the target, R_{ref}, (which in this case corresponds to the center of the scene) are constant over the acquisition period. Each velocity estimate is mapped to its relative acquisition time based on the time vector described in Section 2.2. To enhance visualization in the time domain without altering the signal bandwidth, the discrete velocity vector is upsampled using Whittaker–Shannon (sinc) interpolation [48].

2.2.5. Summary of the Processing Chain. The key steps of the algorithm are illustrated in Figure 5, where, for clarity, the method is applied to a small region of interest (ROI) on one side of the bridge deck. The full processing workflow is summarized as follows:

1. Start from the full-aperture SLC image.
2. Apply an FFT along azimuth to transform the image to the range–azimuth frequency domain.
3. Divide the azimuth spectrum into, N, subapertures using parameters α and Ω (equation (5)).
4. Apply zero padding to maintain the original image dimensions and then perform IFFT to return each subaperture to the range-azimuth domain.
5. Track the azimuth displacement of bright targets across subapertures using 2D cross-correlation.
6. Convert azimuth shifts into LOS velocity using equation (7); optionally, apply sinc interpolation to increase the apparent sampling rate of the velocity time series.

2.3. Case Study: South Portland St. Suspension Bridge. The South Portland Street Suspension Bridge is a historic pedestrian suspension bridge spanning River Clyde in Glasgow, Scotland, UK. It connects the 'City Centre' district on the north bank to the southern districts of Laurieston and the Gorbals. Constructed between 1851 and 1853, the bridge was designed by engineer George Martin in collaboration with architect Alexander Kirkland. Originally constructed from wrought iron, the bridge has undergone several modifications, most recently in 2004 [49].

The bridge features a single main span of 128 m and a deck width of 4.8 m (of which 4.3 m is walkable), as shown in the technical drawings in Figure 6. The deck is suspended from four chains (two on each side), anchored into the ground, and supported by two sandstone towers located at the ends of the span. Figure 7 shows an aerial view of the bridge across River Clyde, along with views from the top and underside of the deck. The maximum sag of the chains at the mid-span is approximately 10.25 m. Each side of the bridge is supported by a total of 77 vertical hangers, which are alternately connected to the upper and lower chains along the span of the bridge. The chains themselves are constructed with differing specifications:

- Lower chain: It is composed of five wrought iron plates, each measuring 100 mm × 25 mm.
- Upper chain: It is composed of four wrought iron plates, each measuring 106 mm × 32 mm (this detail is reported in Figure 6(c)).

The chain node center points are equally spaced at 3.37 m as measured along a chain. As a result, the spacing between the hangers gradually decreases from the center toward the towers as the inclination of the chain increases. Specifically, the horizontal spacing between adjacent hangers varies from 1.68 m at mid-span to 1.61 m near the towers. The distance from the last hanger to the tower is approximately 0.96 m. The bridge deck consists of steel truss elements supporting a wooden walkway, which is then covered by a layer of bituminous pavement. The total mass of the bridge,

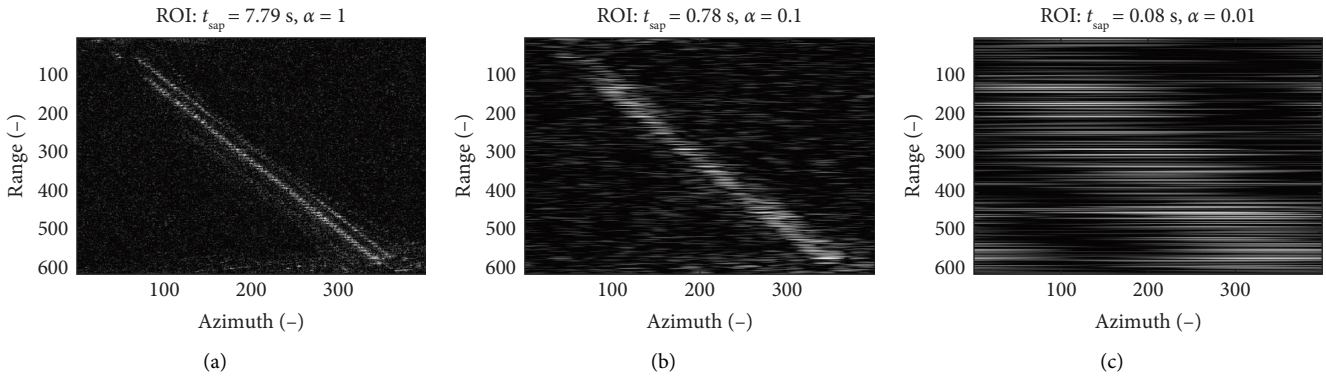

FIGURE 4: The effect of the aperture fraction, α, on the achieved azimuth resolution in a SAR image of the South Portland St. Suspension Bridge: (a) full-aperture image α = 1; (b) subaperture with α = 0.1; (c) subaperture with α = 0.01.

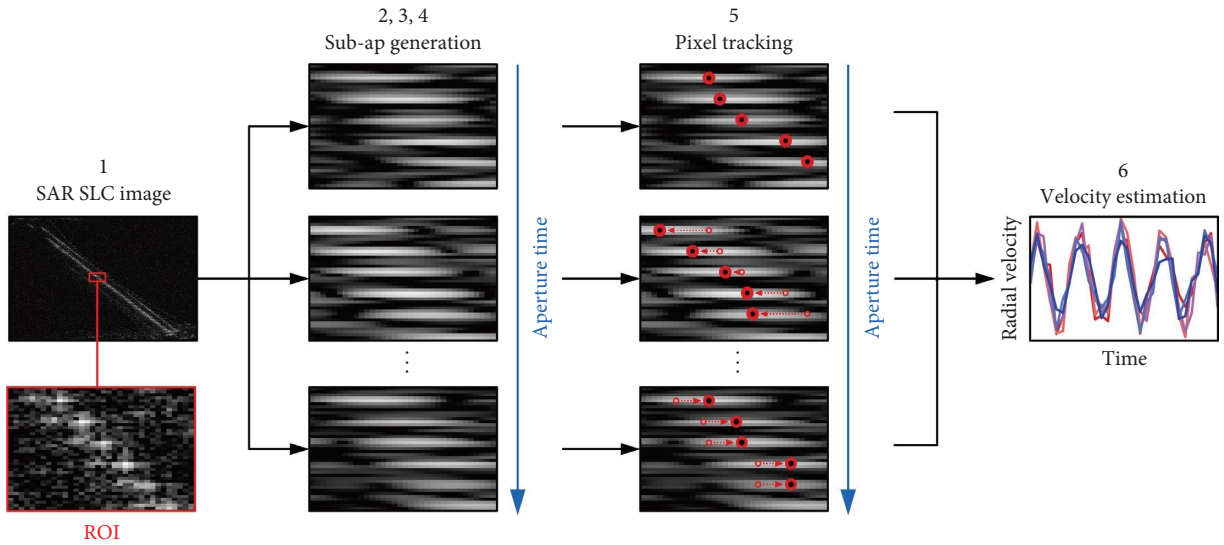

FIGURE 5: Flowchart of the SPOT processing algorithm used to extract radial velocity time histories from SLC spotlight SAR images. The sequence illustrates the workflow described in the summary of the processing chain.

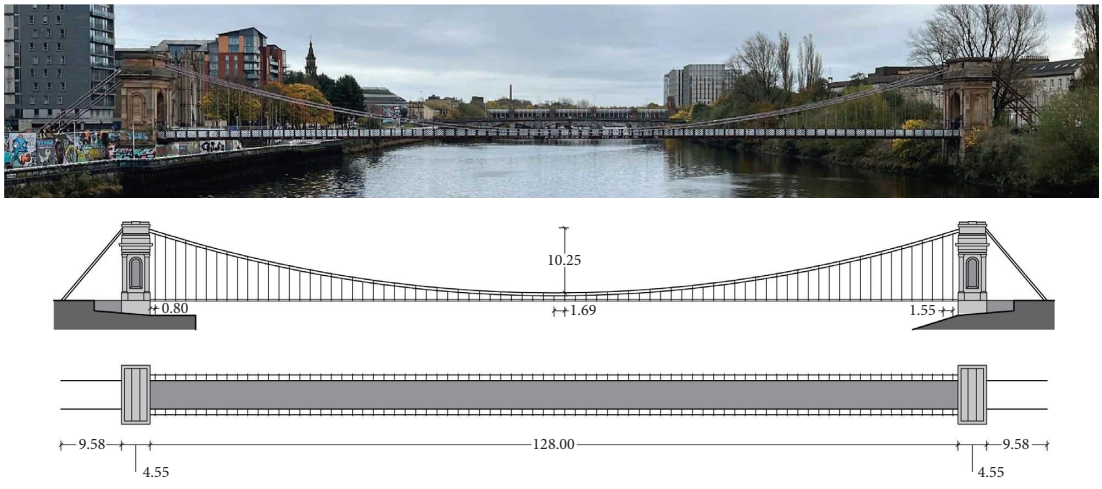

(a)

FIGURE 6: Continued.

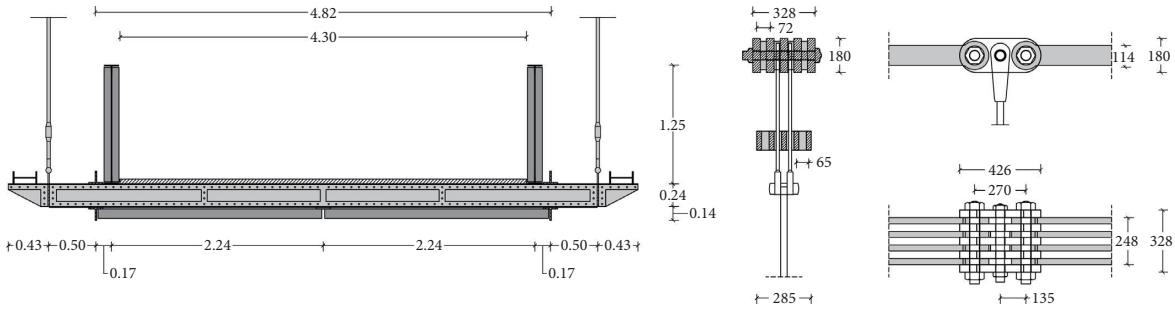

(b) (c)

FIGURE 6: Technical drawings of the South Portland Street Suspension Bridge: (a) side view showing the span and sandstone towers over River Clyde in Glasgow; (b) cross-sectional view of the deck; and (c) detail of the top chain connection, with dimensions in millimeters.

(a) (b) (c)

FIGURE 7: Overview and structural details of the bridge: (a) aerial view of the bridge; (b) view along the top of the bridge deck; (c) view of the underside of the steel truss deck structure.

supported by the four chains, has been estimated to be approximately 131.2 t (including the weight of the chains). The main structural characteristics of the South Portland Street Suspension Bridge are summarized in Table 2:

The South Portland Street Suspension Bridge was selected as a case study for several reasons. First, the bridge is highly reflective in SAR images due to its steel structure and the presence of sharp features and corners, enhancing its visibility in the reflectivity map. Second, as a pedestrian bridge, it allows for the installation of monitoring equipment without the need for traffic closures, enabling the collection of vibration data under operational conditions without disruption. Finally, the long span of the bridge and its slender structure make it prone to vibrations with relatively low frequencies of oscillations, with natural frequencies ranging from approximately 0.38–2.2 Hz (for further details on the magnitude and frequency of vibrations and mode shapes, see Section 2.4).

TABLE 2: Principal features of the South Portland Street Suspension Bridge.

Characteristic	Description
Name	South Portland St. Suspension Bridge
Location	Glasgow, Scotland, United Kingdom
Coordinates	55°51′17.79″ N, 4°15′20.11″ W
River crossed	River Clyde
Type of bridge	Pedestrian suspension bridge
Materials	Wrought iron with sandstone towers
Main span length	128 m
Bridge width	4.5 m
Number of chains	2 per side
Chain sag	10.25 m
Number of hangers	77 per side

2.4. Operational Modal Analysis (OMA). A preliminary investigation of the suspension bridge dynamics was carried out by installing five pairs of wired accelerometers, Model PCB 393B12 [50], along both sides of the deck. The sensors were placed at intervals of approximately one-sixth of the bridge span, as shown in Figures 8 and 9. To capture both horizontal and vertical modes of vibration, two configurations were used: In Configuration 1 (Figure 8), both lines of accelerometers were installed vertically, while in Configuration 2 (Figure 9), the sensors on the western side were installed vertically and the eastern side sensors horizontally. The ends of the bridge were not instrumented, as a preliminary assessment indicated that the response at the bearings was negligible compared to that of the monitored points. Therefore, the ends were assumed to have zero displacement. Acceleration data were acquired at a sampling rate of 2048 Hz for each sensor over approximately 20 min, during which time the bridge remained open to pedestrian

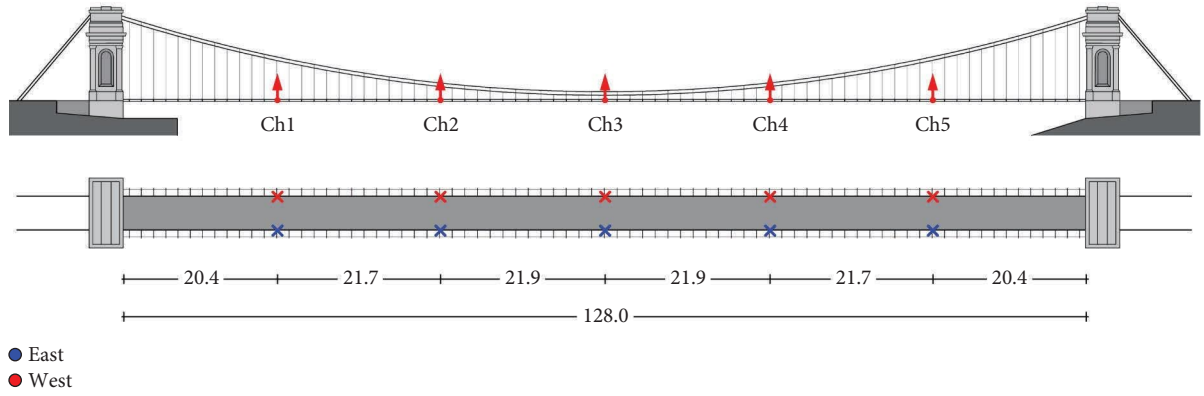

FIGURE 8: Accelerometer configuration—vertical–vertical (VV): schematic layout of the accelerometer installation for Configuration 1. Sensors were placed vertically on both the eastern and western sides of the bridge deck to capture vertical vibrational modes.

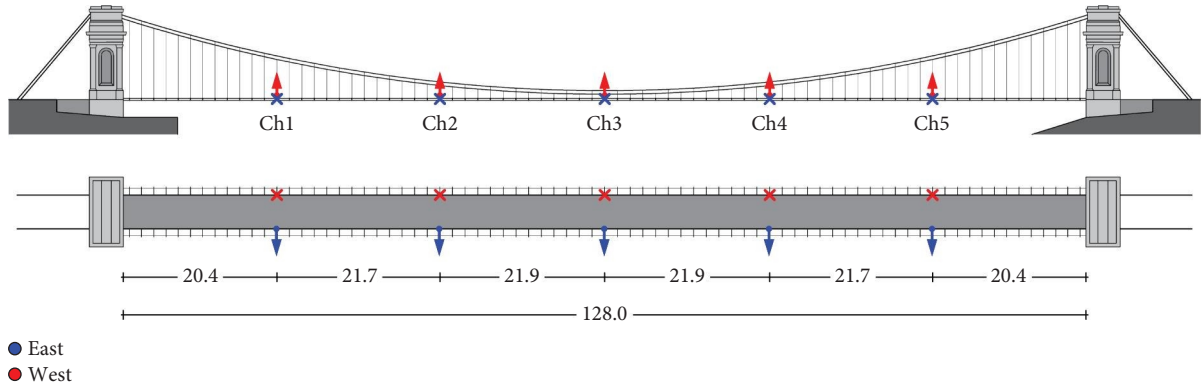

FIGURE 9: Accelerometer configuration—vertical–horizontal (VH): schematic layout of the accelerometer installation for Configuration 2. Vertical sensors were installed on the western side and horizontal sensors on the eastern side to capture both vertical and horizontal modes of vibration.

traffic. Vertical and horizontal acceleration time histories recorded under Configuration 2 are shown in Figures 10 and 11, respectively. To extract the natural frequencies and mode shapes, frequency domain decomposition (FDD) was applied to the collected data [51]. The tool used for the modal extraction was pyOMA, an open-source Python library that enables OMA in both the frequency and time domains [52]. The singular value decomposition (SVD) of the spectral density matrix reveals peaks corresponding to the structural modes at specific frequencies. The evolution of the first three singular values (SVs) is shown in Figures 12(a) and 12(b) for Configuration 1 and Configuration 2, respectively. The figures highlight that, under operational loads, the bridge exhibits the greatest dynamic response within the frequency range of 1.5 – 2.2 Hz. The first nine dominant mode shapes were identified through the FDD technique, and the results are summarized in Table 3. The identified mode shapes along with their associated natural frequencies are shown in Figure 13. It was observed that the bridge mode shapes are predominantly associated with vertical motion. Only the first mode is horizontal, corresponding to the lowest natural frequency of 0.38 Hz. The remaining modes are vertical, consisting of an alternating sequence of flexural and torsional modes. With one exception, these vertical modes show clear sinusoidal deformation patterns along the deck, with the number of nodes increasing from one to three. The single nonsinusoidal mode identified has a frequency of 1.57 Hz.

2.5. SAR Acquisitions and Experimental Validation. This section presents the SAR dataset used in this study and explains how the vibrations measured from SAR imagery were compared to ground-truth data. It first introduces the characteristics of the SAR acquisitions and the parameters used in the SPOT processing chain. Then, it describes the experimental setup, the processing of ground-truth data, and the methodology adopted for validating the performance of the technique.

2.5.1. SAR Data. The SAR dataset used in this work comprises two high-resolution spotlight mode acquisitions provided by Umbra [53], an X-band sensor constellation that delivers data both for public and private use. Both images were delivered as SLC products to preserve m-m effects and were processed independently. Spotlight mode

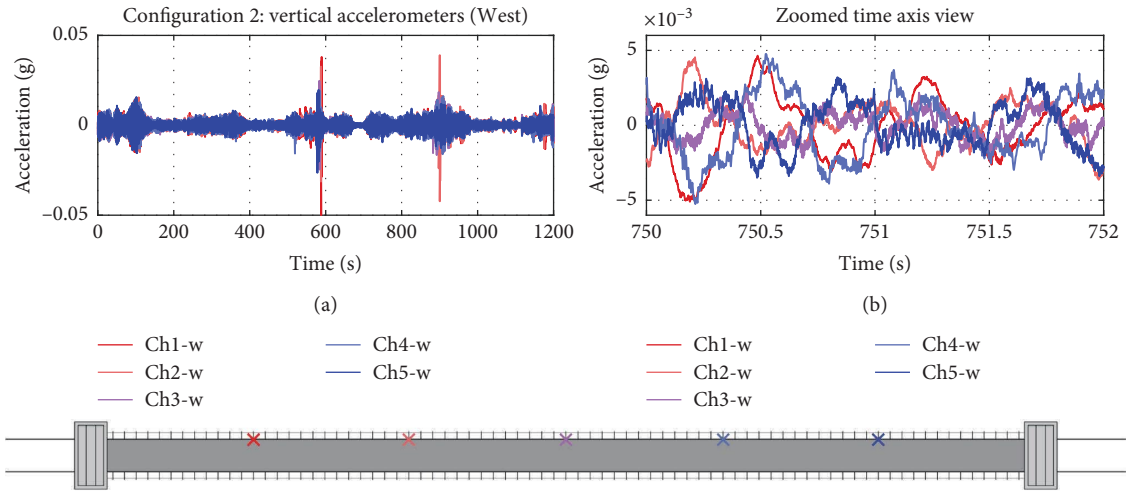

FIGURE 10: Vertical acceleration time history—west side: (a) full 20-min time history recorded by the five vertical accelerometers on the west side during Configuration 2; (b) zoomed-in view.

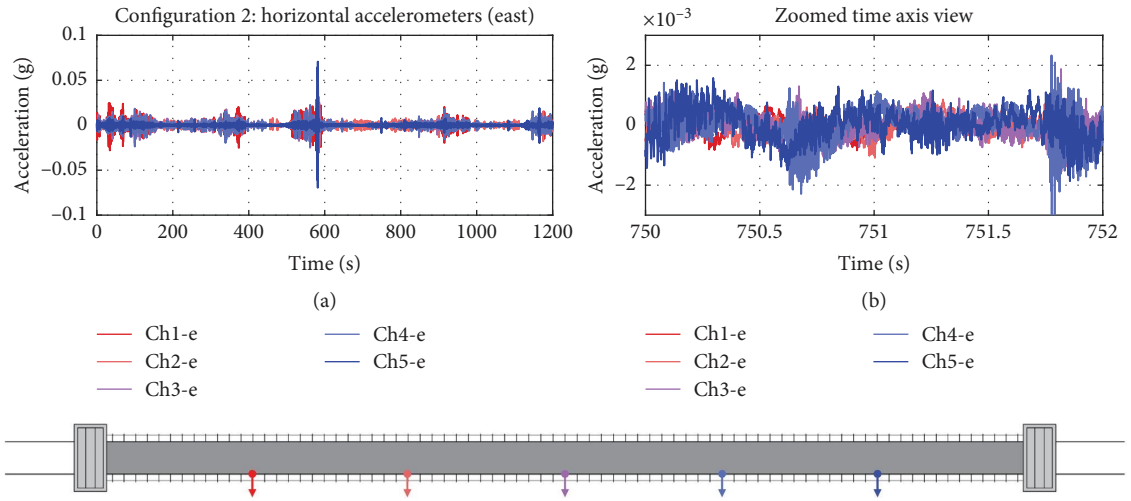

FIGURE 11: Vertical acceleration time history—east side: (a) full 20-min time history recorded by the five vertical accelerometers on the west side during Configuration 2; (b) zoomed-in view.

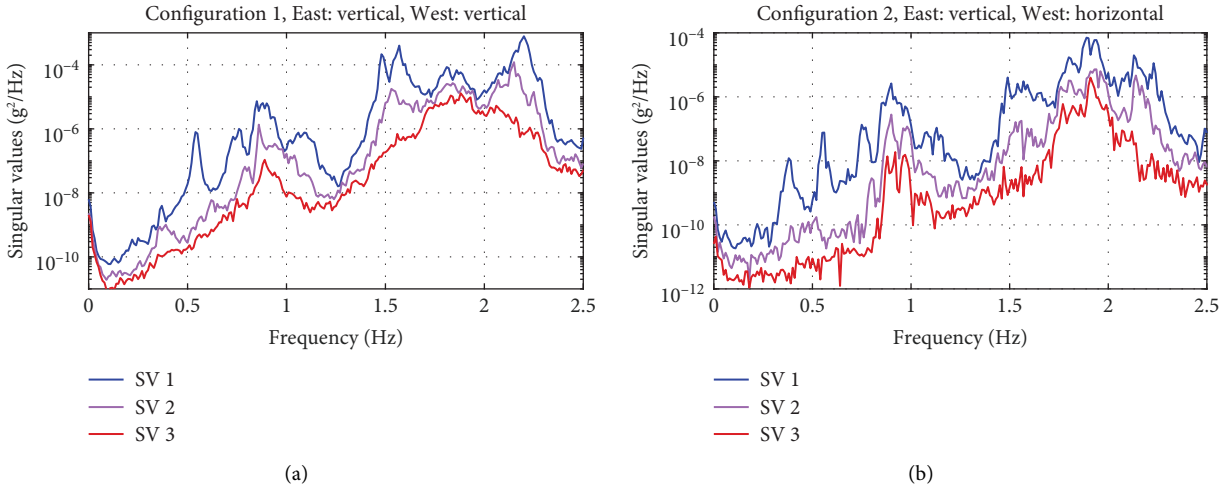

FIGURE 12: SVD of the cross-power spectral density matrix: first three singular values computed via FDD for (a) Configuration 1 (VV May 16 2024 20:00 [UTC]) and (b) Configuration 2 (VH May 16 2024 16:00 [UTC]).

Table 3: Natural frequencies of the bridge case study, resulting from operational modal analysis.

Mode	Direction	Type	Frequency (Hz)
1	Horizontal	Flexural	0.380
2	Vertical	Flexural	0.545
3	Vertical	Torsional	0.753
4	Vertical	Flexural	0.852
5	Vertical	Torsional	1.056
6	Vertical	Flexural	1.481
7	Vertical	Flexural	1.566
8	Vertical	Torsional	1.825
9	Vertical	Flexural	2.215

was selected to maximize the observation time and thus azimuth resolution, as explained previously. Table 4 summarizes the main features of the two SAR acquisitions used in the analysis. Figure 14 illustrates the reflectivity maps of both SAR acquisitions with their corresponding optical images for reference. Figures 14(b) and 14(d) show the SAR reflectivity maps from Acquisition 1 and Acquisition 2, respectively. From the reflectivity maps, the bridge is clearly distinguishable from the water background given due to its stronger backscatter. The most reflective regions of the bridge are near the connections between the hangers and the deck, and near the ends (where the hangers are longer), while the central section appears less reflective in both acquisitions. The two sides of the deck are clearly visible; however, an additional linear feature can be observed, especially in Acquisition 2. This artifact is a mirror image of the structure reflected from the water beneath the bridge. Both edges of the deck are being reflected, but only the near edge (in terms of range) appears distinct from the other features in the SAR image, since the far edge mirror and direct images overlap. This effect must be considered, as water-related backscatter artifacts can introduce noise that affects the velocity extraction. It is acknowledged that this noise will naturally influence the performance of the final results, and in the present work it was not removed.

To measure the SAR time histories, the SPOT method described in Section 2 was used. Table 5 provides a summary of the processing parameters applied to each acquisition. These parameters include the aperture fraction (α), overlap ratio (Ω), number of subapertures (N), and subaperture duration (t_{sap}). Moreover, Table 5 also reports the sampling frequency (f_s) resulting from the parameters, the resolution in the frequency domain (Δf), and the peak mean values of the ground velocities $v_{g,\max}$ for each acquisition. Target pixels for the MDSAR analysis are selected based on consistent reflectivity and the presence of vibrational signatures.

2.5.2. Experimental Comparison. The time histories measured by SAR and the resultant spectra were then compared against ground truth measurements obtained by accelerometers. To capture the full three-dimensional dynamic response, Configuration 2 was adopted (Figure 9), which included one row of vertical and one of horizontal accelerometers (as shown in Figures 15(a) and 15(b)). It was assumed that the horizontal accelerations at both the west and east sides of the deck were identical and that the structural response along the longitudinal direction of the bridge was negligible. Based on this setup, a 20-min acquisition was performed at a sampling rate of 2048 Hz, during which time acceleration data were recorded from the 10 sensors. The acquisition window was centered around the satellite passage to ensure synchronous data collection. To compute the velocities from the acceleration measurements, the acceleration signals were numerically integrated. Prior to integration, a sixth-order Butterworth band-pass filter with cutoff frequencies of 0.1 and 20 Hz was applied. To avoid introducing phase distortion, zero-phase filtering was performed by processing the data in both the forward and backward directions. The resulting vertical and horizontal velocity components were projected along the satellite LOS direction to yield the radial velocities, accounting for the azimuth and incidence angles during the acquisition. The scheme for the velocity projection is illustrated in Figure 15. Finally, the 20-min radial velocity time histories were cropped to match the time of the satellite passage.

Because the radial velocity measurements were available only at a few discrete points, specifically at every sixth of the span, the full velocity profile was reconstructed by interpolating the data through a superposition of the nine mode shapes shown in Figure 13, with equal weighting assigned to each mode during the fitting along the bridge deck. The reconstructed ground-truth radial velocities were assigned to each of the extracted pixel locations, corresponding to the points used in the MDSAR analysis. From these, pixel velocity time histories and ground-truth measurements were compared using Pearson's correlation coefficients and root mean square error (RMSE) to quantitatively assess the performance and accuracy of the SPOT method on a real-world case study.

3. Results and Discussion

This section presents the results obtained using the SPOT technique, comparing the LOS velocity time histories measured from SAR imagery with synchronous ground-truth measurements. For brevity, only three representative time histories per acquisition are reported. The results are discussed separately for Acquisition 1 and Acquisition 2 in the following sections.

3.1. Acquisition 1. Data for Acquisition 1 were collected over an acquisition time $t_a = 7.50$ s. As reported in Table 5, the results were computed with an aperture fraction of $\alpha = 4.14\%$, corresponding to a subaperture duration of $t_{\text{sap}} = 0.31$ s. The overlap ratio Ω was set to 24%, resulting in a sampling frequency of 4.15 Hz, which was then upsampled by a factor of 20 using sinc interpolation. A patch size of 7 pixels in azimuth and 1 pixel in the range was used for cross-correlation tracking. This configuration was selected to ensure tracking accuracy given the expected vibration amplitudes of the bridge deck. Ground measurements indicated peak radial velocities between 0.5 and 2 mm/s, with a mean

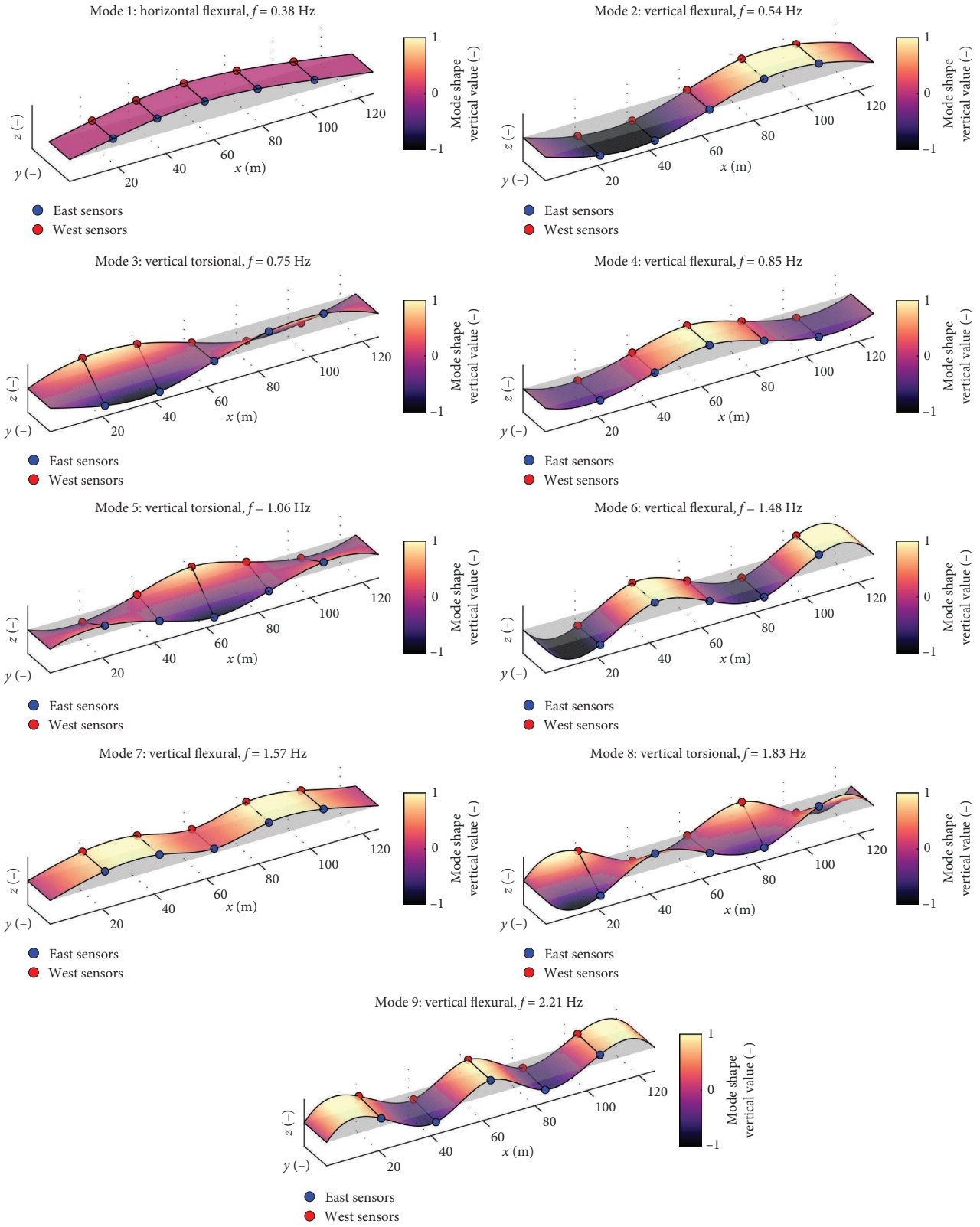

FIGURE 13: Extracted experimental mode shapes: interpolated mode shapes (colored surfaces) identified through OMA-FDD; the color highlights the vertical component of the deformation; east (blue) and west (red) markers indicate sensor positions.

Table 4: Principal features of the SAR acquisitions over the South Portland St. Suspension Bridge.

Quantity	Acquisition 1	Acquisition 2
Date	May 20, 2024	May 16, 2024
Time (UTC)	21:40:40	20:21:23
Acquisition time t_a	7.50 s	16.38 s
Center frequency f	9.6 GHz	9.6 GHz
Wavelength λ	31 mm	31 mm
Pulse repetition frequency (PRF)	4.96 kHz	6.05 kHz
Satellite velocity v_p	7.65 km/s	7.67 km/s
Slant range R_{ref}	765 km	768 km
Incidence angle θ	56.45°	47.67°
Range resolution Δy	18.8 cm	66.8 cm
Azimuth resolution Δx	19.5 cm	8.3 cm

maximum value of $v_{g,\max} = 1.58$ mm/s (as reported in Table 5).

Figure 16 shows the LOS velocity time histories for three representative measurements made from different locations along the deck, with the corresponding ground-truth data. These show that the SAR measured velocities approximately match the oscillatory behavior observed in the ground-truth data; however, the velocity magnitudes are generally overestimated. To evaluate the agreement of the signals in the time domain, two metrics were used: the Pearson's correlation coefficient (ρ_t) and the RMSE, both of which are reported in each subfigure. Starting with Figure 16(a), it is possible to observe that the MDSAR technique successfully captures the decreasing velocity magnitude from approximately 2 to 0.5 mm/s, supporting the similarity between the two curves. The time-domain signals are, however, visibly affected by noise. This is reflected in the RMSE values, which range between 0.7 and 1.4 mm/s (40.1%–76.1% of the maximum ground-truth peak velocity), indicative of the challenges in measuring the precise time history of velocity. The temporal correlation ρ_t values calculated from the SAR and ground-truth measurements are reasonable, with coefficients ranging from 0.46 to 0.66. In the frequency domain, performance was assessed using the absolute frequency error (ϵ_f), estimated as the residual between the highest amplitude frequency components of the SAR and ground-truth measurements, and the Pearson's correlation coefficients of the respective spectra (ρ_f).

These metrics are also reported in the figures presenting the SAR measurement results. Figure 16 shows that the dominant peaks identified in the SAR spectra align well with those from ground truths. The residual error in the estimation of the dominant frequency ranged from 0.04 to 0.10 Hz, which is well within the spectral resolution of $\Delta f = 0.14$ Hz (limited by the short acquisition duration). For the sake of clarity, *dominant frequency* refers to the frequency that is most prominent (i.e., more visible) in the particular signal. Additional low-frequency components also appear in the SAR spectra. While some of these are likely spurious (e.g., the lower-frequency peaks below 0.50 Hz), minor peaks around 0.75 Hz are consistent with those observed in the ground-truth data (e.g., Figures 16(a) and 16(b)). Nonetheless, the overall spectral agreement remains fairly strong, supported by high frequency-domain correlation values of $\rho_f = 0.73$ to 0.88.

These results are consistent across all measured pixels. Figure 17(a) shows the spatial location of all processed pixels, and Figures 17(b) and 17(c) show the values of correlations, with a mean ρ_t of 0.48 and ρ_f of 0.74, aligning with the representative examples. Subsequently, the analysis investigated whether the observed vibrations were consistent with the expected modal behavior of the bridge. The cross-power spectral density (CPSD) matrix was computed from the full set of SAR-measured time histories. SVD processing was then applied to this matrix, following the approach of classical FDD used in OMA [51]. Figure 17(d) compares the first SV associated with SAR measurements to that obtained from the ground-truth data. The two curves exhibit a strong similarity near the dominant frequency peak, with a residual error $\epsilon_f = 0.10$ Hz that is again within spectral resolution limits. The SAR SV amplitude is overestimated, likely due to residual noise. It is worth noting that the frequency peak appears broad in both SAR and ground-truth datasets, suggesting possible modal coupling—where vibrational modes with closely spaced natural frequencies interact and prevent full separation.

3.2. Acquisition 2. Data for Acquisition 2 were collected over an observation time of $t_a = 16.54$ s, which was more than twice that of Acquisition 1. SAR time histories of velocity were measured using an aperture fraction α of 3.54%, comparable to the one used for Acquisition 1, resulting in a subaperture duration of $t_{\text{sap}} = 0.59$ s (which is greater than Acquisition 1, due to the longer t_a). The overlap ratio Ω was increased to 71%, yielding a sampling frequency f_s of 5.87 Hz. As for Acquisition 1, the signal was upsampled by a factor of 20 using sinc interpolation. A patch size of 7 pixels in azimuth and 1 in the range was used, consistent with the configuration in Acquisition 1. Ground-truth measurements indicated similar vibrational amplitudes as those observed in Acquisition 1, with a mean peak radial velocity $v_{g,\max} = 1.29$ mm/s (see Table 5). In this case, fewer valid pixels were identified for measurement. This reduction was primarily due to reduced deck visibility in the SAR image and a coarser range resolution Δy, which limited the number of pixels on the target.

Figure 18 shows the time histories and spectra of the measured radial velocities for three representative pixels, one from the southern end and two from the northern end of the deck. As for Acquisition 1, the time histories show similar issues related to noise. The RMSE values range from 1.0 to 1.1 mm/s, comparable to those observed in the first acquisition. Due to the slightly lower peak velocities in this dataset, the corresponding RMSE percentages are higher, ranging from 73% to 95%. Temporal correlation coefficients ρ_t are slightly lower than those in the previous case, ranging from 0.35 to 0.41, with a mean value of 0.38 (compared to 0.48 for Acquisition 1). Despite the lower correlation and

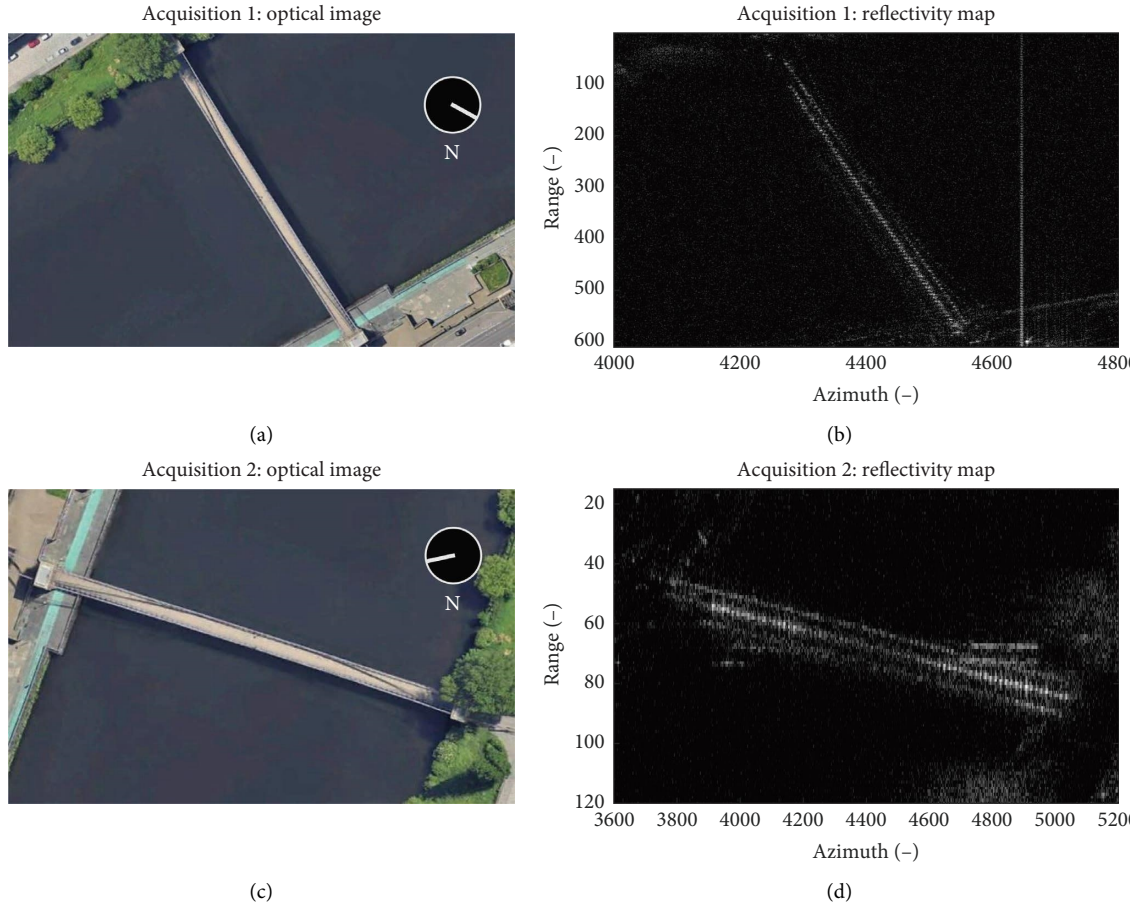

Figure 14: Comparison between optical and SAR imagery of the bridge: (a) optical image for Acquisition 1; (b) reflectivity map from SAR Acquisition 1; (c) optical image for Acquisition 2; (d) reflectivity map from SAR Acquisition 2.

Table 5: SPOT extraction parameters and resulting velocity time history features.

Acquisition (-)	Peak vel. $v_{g,max}$ (mm/s)	Acq. time t_a (s)	Aperture frac. α (%)	Overlap Ω (%)	Sub-ap. number N (-)	Sub-ap. dur. t_{sap} (s)	Samp. freq. f_s (Hz)	Freq. res. Δf (Hz)
1	1.58	7.50	4.14	24.0	31	0.31	4.15	0.14
2	1.29	16.54	3.54	71.0	93	0.59	5.87	0.06

higher error, the SAR measurements still captured the oscillatory behavior, maintaining phase alignment with the ground-truth signals.

The power spectral density comparison also produced coherent results (see Figure 19). The first SV of the CPSD matrix, computed across all SAR-measured time histories, aligns well with the corresponding SV from the ground-truth data. The most dominant frequency peak is captured accurately, with a residual error of $\epsilon_f = 0.03$ Hz, well below the spectral resolution threshold. Moreover, the SAR SV spectrum exhibits secondary peaks in the 0.76 – 0.89-Hz range, consistent with modal components observed in the ground-truth signals and possibly associated with the lower frequency modes of the bridge.

3.3. Discussion. Three main research questions were posed at the beginning of this paper and are answered here based on the results presented.

3.3.1. Can MDSAR Measure the Vibrations of a Real-World Structure? Yes—the experiments demonstrate that MDSAR is unequivocally capable of measuring the vibrations of a real-world bridge. No devices were installed on the structure to enhance target reflectivity during SAR collections. SAR measurements showed oscillatory behavior consistent with the synchronous ground-truth measurements, and spectral peaks from the SAR data aligned closely with the ground-truth data, although some overestimation of velocity values was observed.

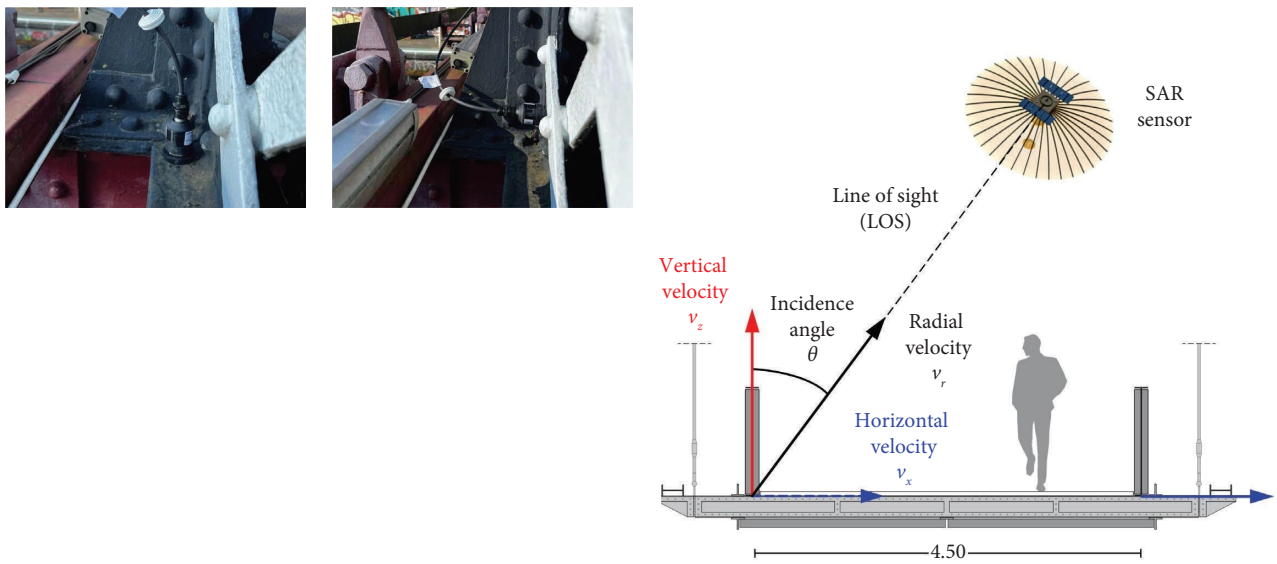

FIGURE 15: SHM system and velocity projection method: (a) vertical accelerometer setup; (b) horizontal accelerometer setup; (c) illustration of radial velocity projection from vertical and horizontal ground velocities using known satellite LOS geometry. The SAR sensor image is adapted from SatNOGS [54].

3.3.2. How Accurate Is the Method, and What Are Its Limitations? The discussion on the accuracy of the method and its limitations are tied in the context to the specific experimental conditions and scenario of the case study, which was a full-scale suspension bridge with vibrational peak velocities along the LOS ranging from 1 to 2 mm/s and dominant frequencies around 1.5 – 2 Hz. However, it is expected that the conclusions are applicable to similar structures.

The measured LOS velocity time histories and corresponding spectra captured the main characteristics of the bridge dynamics. In general, SAR measurements showed vibration patterns consistent with the ground truth, including visible phase alignment. The RMSE remained consistent at approximately 1 mm/s across both acquisitions and at different points along the deck, aligning with previously published results focusing on controlled experiments with isolated targets [40]. It was also observed that SAR measurements tend to overestimate overall velocity amplitudes. The relative error may be considered small or large depending on the amplitude of the vibrations being measured. For these measurements, the RMSE corresponded to 40% and 95% of the true peak velocity for Acquisitions 1 and 2, respectively, which was again consistent with previous CR experimentation [40]. This resulted in temporal correlation values for the two acquisitions averaging to 0.38 and 0.48 (with the best individual pixel value reaching 0.66) for all pixels. On the other hand, spectral correlation coefficients were higher, reaching mean values of 0.65 and 0.74 (with a maximum of 0.88). It is expected that better quality results could be achieved when the bridge vibration velocities are greater in magnitude.

In general, the noise amplitude expected from this technique depends primarily on the following:

- The radar wavelength (λ)—longer wavelengths result in a coarser azimuth resolution (Δx, see equation (1)), which increases tracking error.
- The subaperture duration t_{sap}—where shorter subapertures worsen azimuth resolution, as shown in equation (1).
- The implementation of the tracking algorithm.

In addition to coarse azimuth resolution reducing tracking precision, it also reduces tracking accuracy especially in dense urban environments when multiple closely spaced scattering points are present (known as 'cluttered' environments [36]) due to the increased risk of confusion between poorly resolved targets. Preserving a fine azimuth resolution is therefore essential. Moreover, the use of masking techniques can help identify and exclude areas or features in the SAR imagery that may interfere with the analysis or lead to false interpretations, such as the noise introduced by water backscatter. As for the wavelength, current commercial missions do not offer sensing at shorter wavelengths than X-band ($\lambda = 24 - 38$ mm), but future missions may provide this capability. As for subaperture duration, this is limited by the sampling period and by the overlap ratio. The sampling period must satisfy the Nyquist criterion and thus has to be shorter than half the minimum vibration period of interest. Also, the overlap ratio must be smaller than 100%. Therefore, the sub-aperture duration must necessarily remain shorter than the primary vibrational period of the structure. Finally, improving the

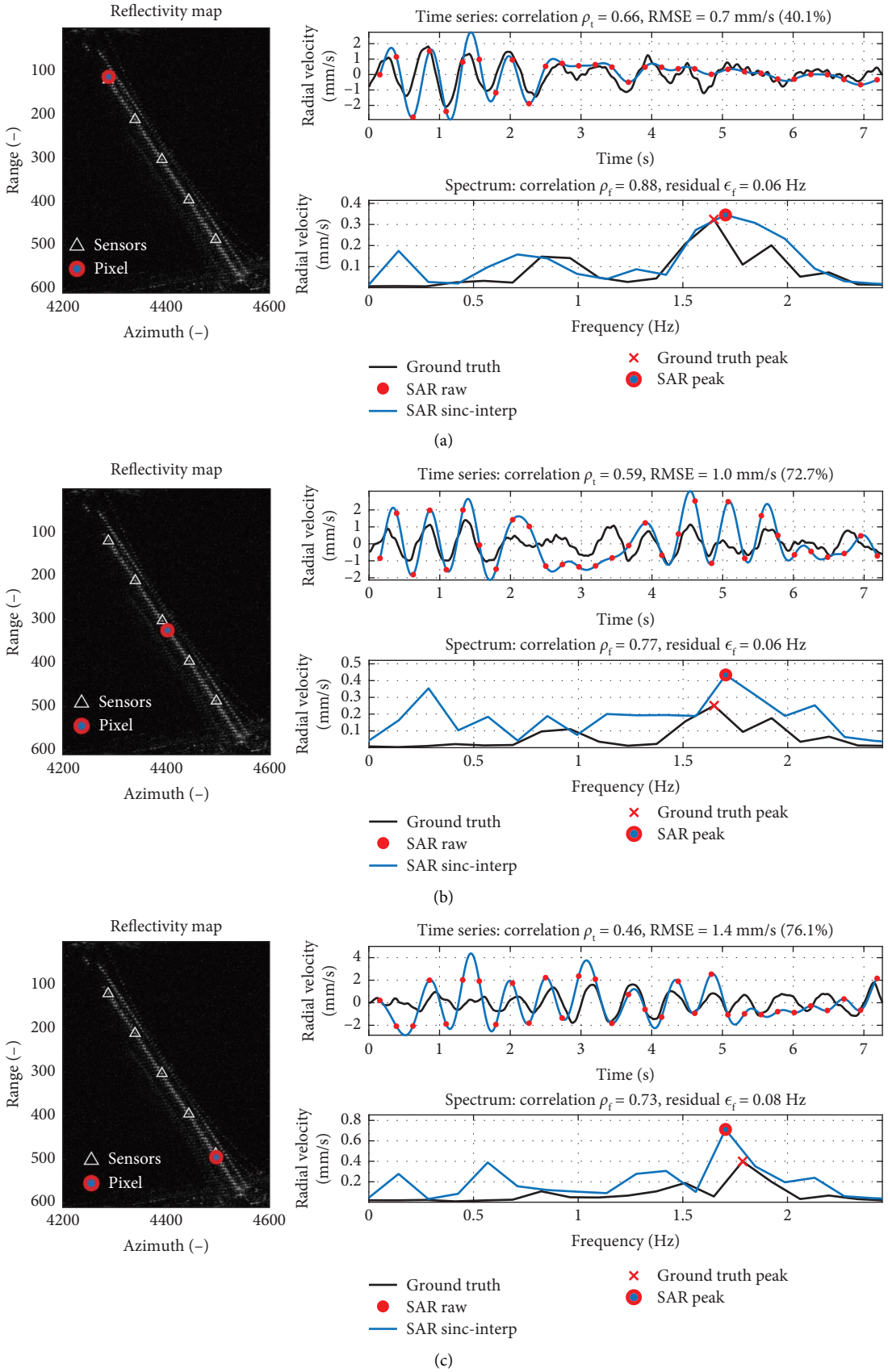

FIGURE 16: Acquisition 1—pixel location, SAR measured LOS velocity, and velocity spectrum compared to ground-truth measurements of (a) Pixel 1, (b) Pixel 2, and (c) Pixel 3. RMSE, frequency error ϵ_f, and time/frequency correlation values are included.

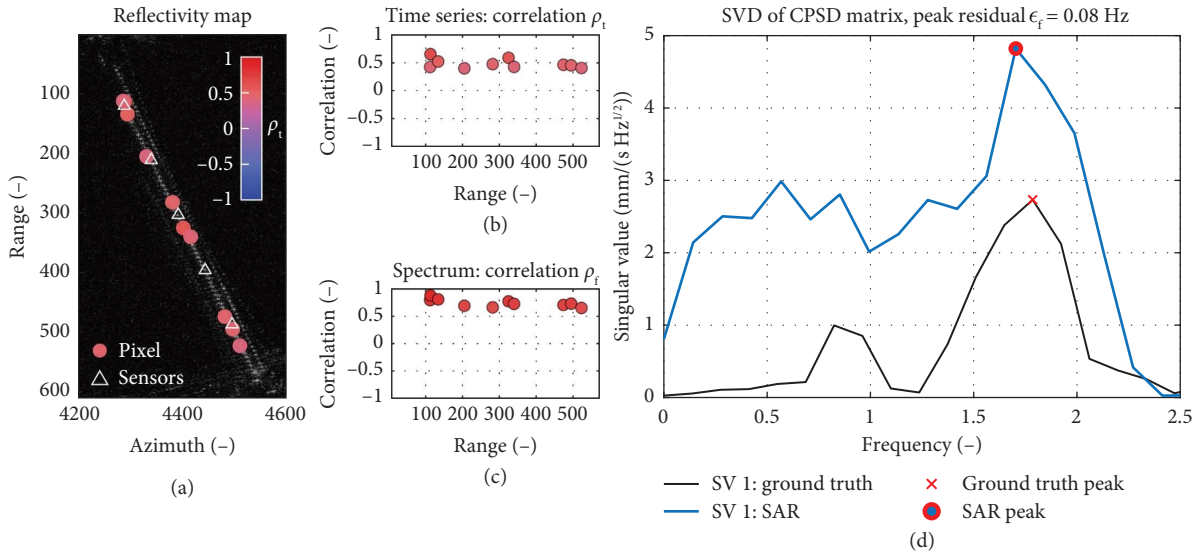

FIGURE 17: Acquisition 1—measurement position overview and CPSD comparison: (a) locations of extracted pixels; (b) time-domain correlation and (c) frequency-domain correlation; (d) first SV of the SAR and ground-truth CPSD matrices. The frequency residual ϵ_f is included.

tracking algorithm, either by optimization or by substitution with more advanced techniques than SPOT, could reduce measurement errors.

3.3.3. Will It Be Possible to Extract Modal Parameters From Spaceborne SAR Data? The principal limitations on the use of MDSAR for the extraction of modal parameters are as follows: the noise level and the short acquisition times available from spaceborne platforms. These factors restrict the extent to which a modal extraction can be performed.

Starting with the measurement of natural frequencies, the first observation is that the MDSAR spectra are consistent with the ground-truth data and dominant frequency peaks are successfully identified from both acquisitions. Specifically, absolute frequency errors range from 0.03 to 0.10 Hz, below the spectral resolution (Δf) in all cases. The correlation in the frequency domain is very satisfactory, with mean values ranging from 0.65 to 0.74, indicating that the spectra are very similar. The peak frequencies of the SVs show strong agreement with those obtained through conventional OMA, indicating that the SAR data can reliably detect dominant frequencies. For example, for Acquisition 2, the first SV reveals a sharp peak at 1.59 Hz, matching the 7th OMA mode at 1.58 Hz and featuring a frequency resolution of 0.06 Hz (comparable to errors observed in other VBSHM techniques). This result was validated using the synchronous ground-truth accelerometers. In contrast, for Acquisition 1, the SV for both the SAR and ground-truth signals (Figure 17(b)), each show a broader dominant peak. This is likely caused by modal coupling of the 1.57- and 1.83-Hz modes, which could not be individually detected due to the limited frequency resolution of both SAR and ground-truth data. The feasibility of the measurement of the natural frequencies via SAR data is inherently constrained by the short observation durations of current commercial satellite missions, which limit the resolution of the frequency spectra. For instance, a 10-s acquisition corresponds to a frequency resolution of ~ 0.1 Hz, which may be insufficient to resolve closely spaced modes, especially in complex structures where modal coupling (e.g., long-span bridges) is present. Furthermore, less excited modes were not observed from the SVs, meaning that vibrations with amplitudes below the measurement accuracy could not be detected. In summary, dominant frequencies can be reliably extracted only when the corresponding modal response along the LOS is comparable to the estimated measurement error and the acquisition duration is sufficient to achieve the desired spectral resolution.

Mode shape identification presents additional challenges, as measurement accuracy plays a more critical role. Effectively, using MDSAR is currently equivalent to using data from very noisy ground-based sensors (with RMSE noise in the order of ~ 1 mm/s) for a short acquisition time (limited to $10-30$ s). Under these conditions, even advanced OMA techniques struggle to distinguish superposed modal responses with high accuracy in the presence of tightly coupled modes. It is expected that modal recognition could possibly be performed, allowing for the separation of different mode shapes and at least the identification of the phase of the modal components. It is also anticipated that accurate mode shape extraction could be possible with an appropriate extraction algorithm that could exploit multiple successive acquisitions of the same target.

The performance of MDSAR in identifying modal parameters could be improved by several strategies. One approach would be the use of CRs to increase reflectivity at specific points on the structure. Placing these at antinodes, where the modal response is the highest, would enhance measurement robustness against clutter and noise. The SAR acquisition geometry could also be optimized in two ways: (i) minimizing the incidence angle (θ) to maximize the projection of vertical velocity along the LOS, therefore

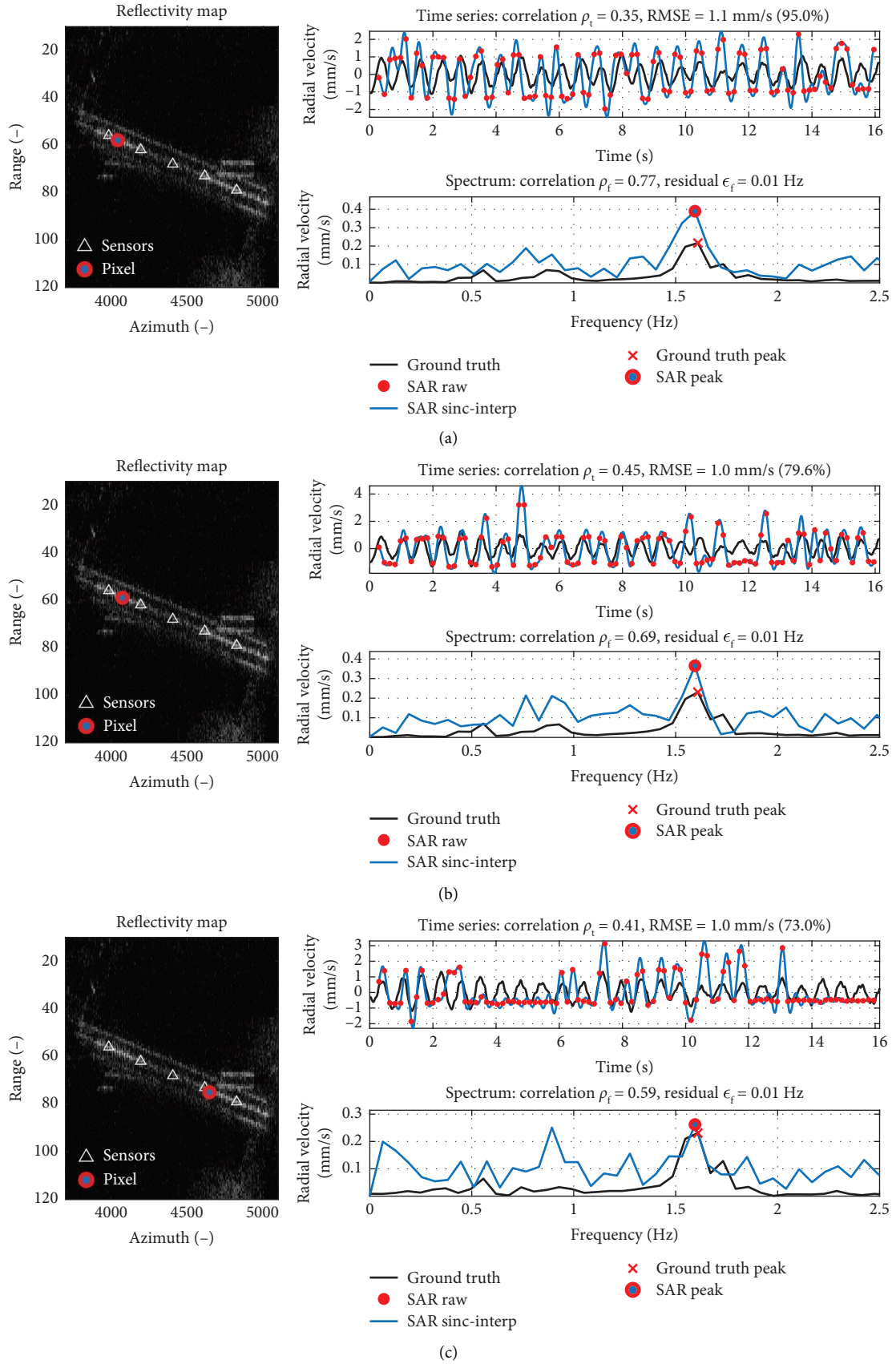

FIGURE 18: Acquisition 2—pixel location, SAR measured LOS velocity, and velocity spectrum compared to ground-truth measurements of (a) Pixel 1, (b) Pixel 2, and (c) Pixel 3. RMSE, frequency error ϵ_f, and time/frequency correlation values are included.

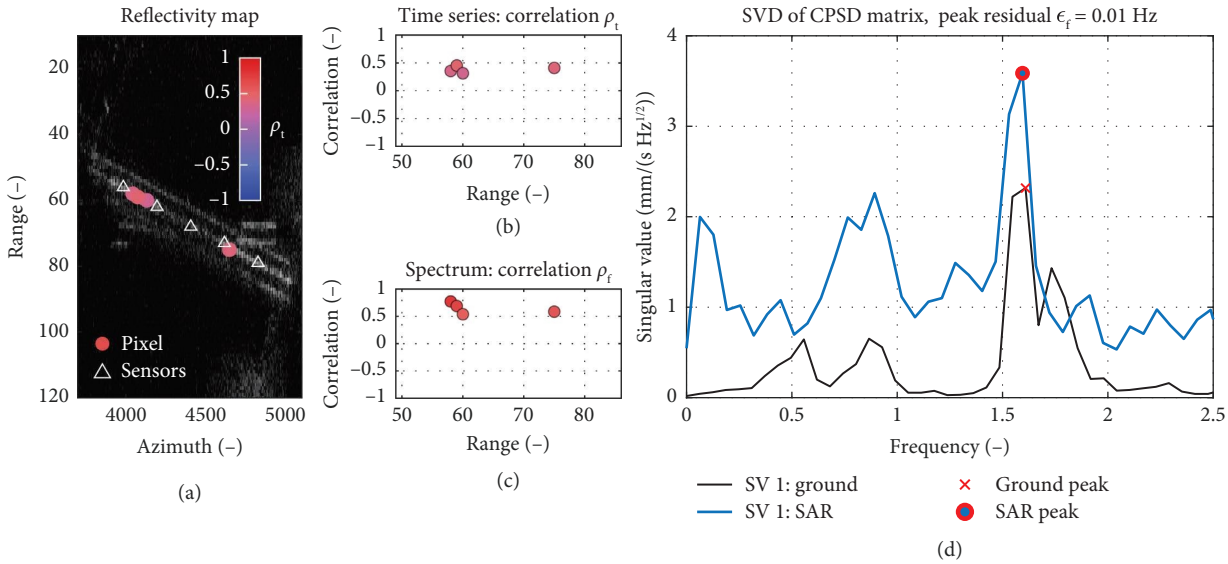

FIGURE 19: Acquisition 2—measurement position overview and CPSD comparison: (a) locations of extracted pixels, (b) time-domain correlation, (c) frequency-domain correlation, and (d) first SV of the SAR and ground-truth CPSD matrices. The frequency residual ϵ_f is included.

improving the m-D measurement sensitivity and (ii) aligning the SAR range axis with the bridge span to maximize the number of independent measurement points along its length. These improvements, however, require control of the satellite orbits and their acquisition parameters. The observation time could be increased to improve frequency resolution through several strategies. Longer duration SAR products (up to ~ 30 s) are already available for specific uses [55]. Additionally, data from multiple acquisitions with consistent geometry and closely spaced in time could be combined to effectively increase the total observation period. This is becoming increasingly feasible as satellite constellations grow, offering more frequent passes. To address the limitations imposed by modal coupling and coarse spectral resolution, super-resolution techniques in the frequency domain, such as MUSIC [56] and ESPRIT [57], could be applied to the measurements made by MDSAR to separate closely spaced frequency components. Another direction could be integrating physical models such as finite element models (FEMs) into the processing pipeline to guide pixel selection and improve tracking results by constraining the solution with additional knowledge of the expected behavior of the target dynamics. Looking further ahead, advances in SAR satellite capabilities, such as longer acquisition durations, shorter revisit times, or higher carrier-frequency sensors providing finer spatial resolution, could support more accurate modal extraction.

4. Conclusions

This work presented an experimental validation and metrological assessment of a MDSAR technique for measuring vibrations from a full-scale suspension bridge. Using high-resolution spotlight SAR imagery, the SPOT algorithm was employed to reconstruct LOS vibration velocity time series of the South Portland St. Suspension Bridge. The results were then compared against synchronous ground-truth measurements collected with a traditional accelerometer system. Based on the experimental results, the following conclusions were drawn:

- The study confirms that MDSAR is indeed capable of measuring real structural vibrations. The SAR measured time histories, and frequency spectra capture the main features of the bridge dynamics.
- The measurement noise of the LOS velocity in the time domain has a standard deviation of approximately 1 mm/s, indicating that the technique is suitable for monitoring structural vibrations with amplitudes greater than this value. In this specific case, where peak velocities of 1.5 – 2 mm/s were recorded, correlation between SAR measurements and ground-truth time histories reached values of up to 0.66, aligning with earlier controlled experiments using CRs.
- The measurement accuracy of the SPOT technique is primarily influenced by the radar wavelength, the subaperture duration, and the efficiency of the subpixel tracking algorithm. While the subaperture duration is limited by the sampling period, future improvements could be obtained by employing satellite missions with shorter wavelengths and by refining pixel tracking techniques. Alternative MDSAR measurement methods, such as those based on measuring signal phase directly, could also be integrated into the measurement pipeline and may yield increased sensitivity.
- The technique presented is effective for estimating the dominant vibrational frequency of the structure, with a frequency resolution that essentially depends on the acquisition duration of the spotlight SAR collection. In this study, resolutions as fine as 0.06 Hz were achieved. With currently available missions, durations up to 30 s

could be, in principle, reached, resulting in a frequency resolution of approximately 0.03 Hz.

- Extracting mode shapes is more challenging. Meaningful results could be obtained in the absence of modal coupling, but the overall performance is limited by short acquisition durations and noise in the velocity time histories.
- It is expected that modal recognition could be performed, and that this would allow the separation of different modes and at least the identification of their phase components. The accurate estimation of mode shapes, however, would require the development of an appropriate extraction algorithm.

In summary, future developments to improve the quality of the MDSAR measurement would involve the testing of other processing strategies developed in the literature, deploying CRs at selected locations to enhance reflectivity, applying masking techniques to reduce noise in SAR imagery, integrating physical models, and exploiting multiple acquisitions to extend effective observation time.

Data Availability Statement

The data that support the findings of this study are available on request from the corresponding author. The data are not publicly available due to privacy or ethical restrictions.

Conflicts of Interest

The authors declare no conflicts of interest.

Funding

The study presented was funded by the European Space Agency under the projects "Bridge Monitoring Based on Single Pass SAR Images" (ESA Contract No. 4000142119) and "EO4Security–Innovative SAR Processing Methodologies For Security Applications-Topic B2: Micro-Doppler Processing" (ESA Contract No. 4000142272/23/I-DT), the ReLUIS Interuniversity Consortium under the agreement DPC-ReLUIS 2020-2022 and DPC-ReLUIS 2024-2026 WP 6 "Monitoring and satellite data", and the European Union–Next Generation EU, Mission 4 Component 2–CUP E53D23003560006.

The work of P.M. was performed at the University of Houston under a contract with the NASA Commercial Smallsat Data Scientific Analysis Program (NNH22ZDA001N-CSDSA), the NASA Commercial Smallsat Data Acquisition New Vendor Onramp Evaluation (NNH23ZDA001N-CNVOE), and the NASA Commercial Satellite Data Earth Science Research and Applications program (NNH24ZDA001N-CESRA). Open access publishing was facilitated by Universita degli Studi di Trento, as part of the Wiley–CRUI-CARE agreement.

Acknowledgments

The authors would like to acknowledge the collaboration of Umbra Space for providing satellite images, Glasgow City Council for authorizing on-site tests, and the University of Trento and the University of Strathclyde for helping with the tests. The authors would also like to thank Ernesto Imbembo, Marc Zimmermanns, and Maria Michela Corvino from the European Space Agency for their support throughout this research.

References

[1] W. Fan and P. Qiao, "Vibration-Based Damage Identification Methods: A Review and Comparative Study," *Structural Health Monitoring* 10, no. 1 (2011): 83–111, https://doi.org/10.1177/1475921710365419.

[2] R. Hou and Y. Xia, "Review on the New Development of Vibration-Based Damage Identification for Civil Engineering Structures: 2010–2019," *Journal of Sound and Vibration* 491 (2021): 115741, https://doi.org/10.1016/j.jsv.2020.115741.

[3] J. J. Moughty and J. R. Casas, "A State of the Art Review of Modal-Based Damage Detection in Bridges: Development, Challenges, and Solutions," *Applied Sciences* 7, no. 5 (2017): 510, https://doi.org/10.3390/app7050510.

[4] Y. Bao and H. Li, "Machine Learning Paradigm for Structural Health Monitoring," *Structural Health Monitoring* 20, no. 4 (2021): 1353–1372, https://doi.org/10.1177/1475921720972416.

[5] S. S. Saidin, A. Jamadin, S. Abdul Kudus, N. Mohd Amin, and M. A. Anuar, "An Overview: The Application of Vibration-Based Techniques in Bridge Structural Health Monitoring," *International Journal of Concrete Structures and Materials* 16, no. 1 (2022): 69, https://doi.org/10.1186/s40069-022-00557-1.

[6] E. Ozer, A. G. Özcebe, C. Negulescu, et al., "Vibration-Based and Near Real-Time Seismic Damage Assessment Adaptive to Building Knowledge Level," *Buildings* 12, no. 4 (2022): 416, https://doi.org/10.3390/buildings12040416.

[7] J. Brownjohn, "Structural Health Monitoring of Civil Infrastructure," *Philosophical Transactions of the Royal Society A: Mathematical, Physical and Engineering Sciences* 365, no. 1851 (2007): 589–622, https://doi.org/10.1098/rsta.2006.1925.

[8] T. Nagayama, S. Sim, Y. Miyamori, and B. J. Spencer, "Issues in Structural Health Monitoring Employing Smart Sensors," *Smart Structures and Systems* 3, no. 3 (2007): 299–320, https://doi.org/10.12989/SSS.2007.3.3.299.

[9] A. Z. E. Foden, in *Value and Challenges of Structural Monitoring for long-span Bridges* (CRC Press, Taylor & Francis Group, 2023).

[10] F. J. Carrión, J. A. Quintana, and S. E. Crespo, "Techno-Economical and Practical Considerations for SHM Systems," *Journal of Civil Structural Health Monitoring* 7, no. 2 (2017): 207–215, https://doi.org/10.1007/s13349-017-0215-x.

[11] D. Li, B. Li, T. Wang, and J. Zhang, "Lightweight Structural Health Monitoring and Safety Evaluation: Review and Case Studies," *Advances in Structural Engineering* 28, no. 12 (2025): 13694332251325043–2179, https://doi.org/10.1177/13694332251325043.

[12] J. Valença, X. Qin, L. Chang, J. Dong, X. Shi, and J. R. Casas, "Remote Sensing-Based Structural Health Monitoring and Damage Assessment," *Remote Sensing* 16, no. 7 (2024): 1146, https://doi.org/10.3390/rs16071146.

[13] T. Panigati, M. Zini, D. Striccoli, et al., "Drone-Based Bridge Inspections: Current Practices and Future Directions," *Automation in Construction* 173 (2025): 106101, https://doi.org/10.1016/j.autcon.2025.106101.

[14] H. Kim and G. Kim, "Reliability Assessment of a Vision-Based Dynamic Displacement Measurement System Using an

Unmanned Aerial Vehicle," *Sensors* 23, no. 6 (2023): 3232, https://doi.org/10.3390/s23063232.

[15] S. Ri, J. Ye, N. Toyama, and N. Ogura, "Drone-Based Displacement Measurement of Infrastructures Utilizing Phase Information," *Nature Communications* 15, no. 1 (2024): 395, https://doi.org/10.1038/s41467-023-44649-2.

[16] T. Miyashita and M. Nagai, "Vibiration-Based Structural Health Monitoring for Bridges Using Laser Doppler Vibrometers and MEMS-Based Technologies," *International Journal of Steel Structures* 8 (2008): 325–331.

[17] E. Kaartinen, K. Dunphy, and A. Sadhu, "LiDAR-Based Structural Health Monitoring: Applications in Civil Infrastructure Systems," *Sensors* 22, no. 12 (2022): 4610, https://doi.org/10.3390/s22124610.

[18] A. Trias-Blanco, J. Gong, and F. L. Moon, "Characterization of Operational Vibrations of Steel-Girder Highway Bridges via LiDAR," *Remote Sensing* 15, no. 4 (2023): 1003, https://doi.org/10.3390/rs15041003.

[19] S. Sotoudeh, L. Lantini, S. Uzor, and F. Tosti, "A Systematic Review Into the Application of Ground-Based Interferometric Radar Systems for Bridge Monitoring," *Remote Sensing* 17, no. 9 (2025): 1541, https://doi.org/10.3390/rs17091541.

[20] C. Michel and S. Keller, "Advancing Ground-Based Radar Processing for Bridge Infrastructure Monitoring," *Sensors* 21, no. 6 (2021): 2172, https://doi.org/10.3390/s21062172.

[21] A. Beni, L. Miccinesi, L. Pagnini, A. Cioncolini, J. Shan, and M. Pieraccini, "Interferometric Radars for Bridge Monitoring: Comparison Among X-Bands, Ku-Bands, and W-Bands," *Remote Sensing* 16, no. 17 (2024): 3323, https://doi.org/10.3390/rs16173323.

[22] D. Amitrano, G. Di Martino, R. Guida, et al., "Earth Environmental Monitoring Using Multi-Temporal Synthetic Aperture Radar: A Critical Review of Selected Applications," *Remote Sensing* 13, no. 4 (2021): 604, https://doi.org/10.3390/rs13040604.

[23] E. S. Agency, "Sentinel-1," (2025), https://www.esa.int/Applications/Observing_the_Earth/Copernicus/Sentinel-1.

[24] G. Chen, Y. Zhang, R. Zeng, et al., "Detection of Land Subsidence Associated With Land Creation and Rapid Urbanization in the Chinese Loess Plateau Using Time Series InSAR: A Case Study of Lanzhou New District," *Remote Sensing* 10, no. 2 (2018): 270, https://doi.org/10.3390/rs10020270.

[25] K. Malik, D. Kumar, D. Perissin, and B. Pradhan, "Estimation of Ground Subsidence of New Delhi, India Using PS-InSAR Technique and Multi-Sensor Radar Data," *Advances in Space Research* 69, no. 4 (2022): 1863–1882, https://doi.org/10.1016/j.asr.2021.08.032.

[26] X. Qin, M. Liao, M. Yang, and L. Zhang, "Monitoring Structure Health of Urban Bridges With Advanced Multi-Temporal InSAR Analysis," *Annals of GIS* 23, no. 4 (2017): 293–302, https://doi.org/10.1080/19475683.2017.1382572.

[27] D. Tonelli, V. F. Caspani, A. Valentini, et al., "Interpretation of Bridge Health Monitoring Data From Satellite InSAR Technology," *Remote Sensing* 15, no. 21 (2023): 5242, https://doi.org/10.3390/rs15215242.

[28] P. Milillo, R. Bürgmann, P. Lundgren, et al., "Space Geodetic Monitoring of Engineered Structures: The Ongoing Destabilization of the Mosul Dam, Iraq," *Scientific Reports* 6, no. 1 (2016): 37408, https://doi.org/10.1038/srep37408.

[29] S. Selvakumaran, S. Plank, C. Geiß, C. Rossi, and C. Middleton, "Remote Monitoring to Predict Bridge Scour Failure Using Interferometric Synthetic Aperture Radar (InSAR) Stacking Techniques," *International Journal of Applied Earth Observation and Geoinformation* 73 (2018): 463–470, https://doi.org/10.1016/j.jag.2018.07.004.

[30] P. Milillo, G. Giardina, D. Perissin, G. Milillo, A. Coletta, and C. Terranova, "Pre-Collapse Space Geodetic Observations of Critical Infrastructure: The Morandi Bridge, Genoa, Italy," *Remote Sensing* 11, no. 12 (2019): 1403, https://doi.org/10.3390/rs11121403.

[31] D. Cusson, C. Rossi, and I. F. Ozkan, "Early Warning System for the Detection of Unexpected Bridge Displacements From Radar Satellite Data," *Journal of Civil Structural Health Monitoring* 11, no. 1 (2021): 189–204, https://doi.org/10.1007/s13349-020-00446-9.

[32] T. Carlà, E. Intrieri, F. Raspini, et al., "Perspectives on the Prediction of Catastrophic Slope Failures From Satellite InSAR," *Scientific Reports* 9, no. 1 (2019): 14137, https://doi.org/10.1038/s41598-019-50792-y.

[33] D. Perissin, "Geometric Processing: Active Sensor Modeling and Calibration (SAR)," *Elsevier* (2018): 61–76, https://doi.org/10.1016/b978-0-12-409548-9.10336-7.

[34] V. C. Chen, "The Micro-Doppler Effect in Radar," *Artech House Radar seriesNorwood, MA: Artech House*, 2nd ed. (2019).

[35] M. Ruegg, E. Meier, and D. Nuesch, "Vibration and Rotation in Millimeter-Wave SAR," *IEEE Transactions on Geoscience and Remote Sensing* 45, no. 2 (2007): 293–304, https://doi.org/10.1109/TGRS.2006.887025.

[36] F. Rollo, C. Ilioudis, and C. Clemente, "Advances in Micro-Doppler Processing in Synthetic Aperture Radar: A Review of Techniques, Results, and Future Trends," *IEEE Geoscience and Remote Sensing Magazine* (2025): 2–24, https://doi.org/10.1109/MGRS.2025.3573099.

[37] V. Chen, L. Fayin, H. Shen-Shyang, and H. Wechsler, "Micro-Doppler Effect in Radar: Phenomenon, Model, and Simulation Study," *IEEE Transactions on Aerospace and Electronic Systems* 42, no. 1 (2006): 2–21, https://doi.org/10.1109/TAES.2006.1603402.

[38] C. Clemente, D. Tonelli, A. Lotti, et al., in *On Micro-Motion Extraction From High Resolution X-Band SAR Products* (IEEE, 2024).

[39] F. Rollo, C. V. Ilioudis, G. Zefi, et al., "Micro-Motion Extraction from Spotlight SAR Using a Modified Backprojection Approach," in *Microwave Remote Sensing: Data Processing and Applications IIISPIE*, ed. E. Santi, F. Bovenga, C. Notarnicola, and N. Pierdicca (Edinburgh, United Kingdom: SPIE, 2024), 12.

[40] A. Lotti, A. B. Vattulainen, C. Suppi, et al., "Feasibility of Micro-Motion From SAR Imagery for Vibration-Based SHM," in *SHMII* (Verlag der Technischen Universität Graz, 2025).

[41] F. Biondi, P. Addabbo, C. Clemente, S. L. Ullo, and D. Orlando, "Monitoring of Critical Infrastructures by Micromotion Estimation: The Mosul Dam Destabilization," *Ieee Journal of Selected Topics in Applied Earth Observations and Remote Sensing* 13 (2020): 6337–6351, https://doi.org/10.1109/JSTARS.2020.3030977.

[42] F. Biondi, P. Addabbo, S. L. Ullo, C. Clemente, and D. Orlando, "Perspectives on the Structural Health Monitoring of Bridges by Synthetic Aperture Radar," *Remote Sensing* 12, no. 23 (2020): 3852, https://doi.org/10.3390/rs12233852.

[43] A. Focsa, A. Anghel, G. Nico, I. Maggio, M. Datcu, and M. Corvino, in *Vibration-Induced Micro-Doppler Estimation in Spaceborne SAR Images Using Doppler Centroid Tracking Across Azimuth Sub-Apertures* (IEEE, 2025).

[44] A. B. Vattulainen, F. Rollo, A. Lotti, et al., in *Bridge Vibration Measurements from Very High-Resolution Spaceborne SAR* (IEEE, 2024).
[45] "Earth Science Data Systems N. Synthetic Aperture Radar (SAR) | NASA Earthdata," https://www.earthdata.nasa.gov/learn/earth-observation-data-basics/sar;2021.Publisher:EarthScienceDataSystems,NASA.
[46] A. Moreira, P. Prats-Iraola, M. Younis, G. Krieger, I. Hajnsek, and K. P. Papathanassiou, "A Tutorial on Synthetic Aperture Radar," *IEEE Geoscience and Remote Sensing Magazine* 1, no. 1 (2013): 6–43, https://doi.org/10.1109/MGRS.2013.2248301.
[47] R. Raney, "Synthetic Aperture Imaging Radar and Moving Targets," *IEEE Transactions on Aerospace and Electronic Systems* 7, no. 3 (1971): 499–505, https://doi.org/10.1109/TAES.1971.310292.
[48] C. Shannon, "Communication in the Presence of Noise," *Proceedings of the IRE* 37, no. 1 (1949): 10–21, https://doi.org/10.1109/JRPROC.1949.232969.
[49] "Glasgow, Upper Harbour, South Portland Street Suspension Footbridge | Canmore," (2025), https://canmore.org.uk/site/44349/glasgow-upper-harbour-south-portland-street-suspension-footbridge?utm_source=chatgpt.com.
[50] "Model 393B12 | PCB Piezotronics," (2025), https://www.pcb.com/products?m=393b12.
[51] R. Brincker and C. E. Ventura, *Introduction to Operational Modal Analysis*, 1st ed ed. (Wiley, 2015).
[52] D. P. Pasca, A. Aloisio, M. M. Rosso, and S. Sotiropoulos, "PyOMA and PyOMA_GUI: A Python Module and Software for Operational Modal Analysis," *SoftwareX* 20 (2022): 101216, https://doi.org/10.1016/j.softx.2022.101216.
[53] "Umbra Space. Delivering Global Omniscience Umbra," (2023), https://umbra.space/.
[54] "EoPortal. Umbra SAR Constellation," (2025), https://www.eoportal.org/satellite-missions/umbra-sar#orbit.
[55] "Capella Space. What Are Capella's Collection Types?" (2025), https://support.capellaspace.com/what-are-capellas-collection-types.
[56] R. Schmidt, "Multiple Emitter Location and Signal Parameter Estimation," *IEEE Transactions on Antennas and Propagation* 34, no. 3 (1986): 276–280, https://doi.org/10.1109/tap.1986.1143830.
[57] R. Roy, A. Paulraj, and T. Kailath, "Estimation of Signal Parameters via Rotational Invariance Techniques-ESPRIT," in *SPIE Proceedings. 0696*, ed. J. M. Speiser (SPIE, 1986).